1 **Palaeo-environmental evolution of Central Asia during the Cenozoic: New insights from**

2 **the continental sedimentary archive of the Valley of Lakes (Mongolia)**

3

4 Andre Baldermann[1*], Oliver Wasser[1], Elshan Abdullayev[2,3], Stefano Bernasconi[4], Stefan

5 Löhr[5], Klaus Wemmer[6], Werner E. Piller[7], Maxim Rudmin[8] and Sylvain Richoz[9]

6

7 [1]Institute of Applied Geosciences, Graz University of Technology, NAWI Graz Geocenter, Graz,

8 Austria; baldermann@tugraz.at; oliver.wasser@student.tugraz.at

9 [2]Department of Life Sciences, Khazar University, Baku, Azerbaijan; elabdulla3@gmail.com

10 [3]Department of Geoscience, French-Azerbaijani University (UFAZ), Baku, Azerbaijan;

11 elabdulla3@gmail.com

12 [4]Geological Institute, ETH Zurich, Zurich, Switzerland; stefano.bernasconi@erdw.ethz.ch

13 [5]Department of Earth and Environmental Sciences, Macquarie University, Sydney, Australia;

14 stefan.loehr@mq.edu.au

15 [6]Geoscience Centre (GZG), University of Göttingen, Göttingen, Germany; kwemmer@gwdg.de

16 [7]Institute of Earth Sciences, University of Graz, NAWI Graz Geocenter, Graz, Austria;

17 werner.piller@uni-graz.at

18 [8]Division of Geology, Tomsk Polytechnic University, Tomsk, Russia; rudminma@tpu.ru

19 [9]Department of Geology, University of Lund, Lund, Sweden; sylvain.richoz@geol.lu.se

20

21 *Corresponding author: Andre Baldermann

22 Institute of Applied Geosciences, Graz University of Technology, 8010, Graz, Austria

23 Tel: +43 316 873 6850, Fax: +43 316 873 6876; E-mail: baldermann@tugraz.at

24

25 Key Words: Cenozoic climate change; Central Asia; Palaeo-environment; Westerly winds;

26 Hydroclimate; Paleosols

Abstract

The Valley of Lakes basin (Mongolia) contains a unique continental sedimentary archive, suitable for constraining the influence of tectonics and climate change on the aridification of Central Asia in the Cenozoic. We identify the sedimentary provenance, the (post)depositional environment and the palaeo-climate based on sedimentological, petrographical, mineralogical and (isotope) geochemical signatures recorded in authigenic and detrital silicates as well as soil carbonates in a sedimentary succession spanning ~34 to 21 Ma. The depositional setting was characterized by an ephemeral braided river system draining prograding alluvial fans, with episodes of lake, playa or open steppe sedimentation. Metamorphics from the northern adjacent Neoarchean to late Proterozoic hinterlands provided a continuous influx of silicate detritus to the basin, as indicated by K-Ar ages of detrital muscovite (~798-728 Ma) and discrimination function analysis. The authigenic clay fraction is dominated by illite-smectite and "hairy" illite (K-Ar ages: ~34-25 Ma), which formed during coupled petrogenesis and precipitation from hydrothermal fluids originating from major basalt flow events (~32-29 Ma and ~29-25 Ma). Changes in hydroclimate are recorded in $\delta^{18}O$ and $\delta^{13}C$ profiles of soil carbonates and in silicate mineral weathering patterns, indicating comparatively humid to semi-arid conditions prevailed in the late(st) Eocene, changing into arid conditions in the Oligocene and back to humid to semi-arid conditions in the early Miocene. Aridification steps are indicated at ~34-33 Ma, ~31 Ma, ~28 Ma and ~23 Ma and coincide with some episodes of high-latitude ice sheet expansion inferred from marine deep-sea sedimentary records. This suggests long-term variations of the ocean/atmosphere circulation patterns due to pCO$_2$ fall, re-configurations of ocean gateways and ice-sheet expansion in Antarctica could have impacted the hydroclimate and weathering regime in the basin. We conclude that the aridification in Central Asia was triggered by reduced moisture influx by westerly winds driven by Cenozoic climate forcing and the exhumation of the Tian Shan and Altai mountains and modulate by global climate events.

1. Introduction

The Cenozoic Era (66 Ma to the present day) saw several dramatic changes of the marine and continental ecosystems (e.g., evolution of large plankton feeders such as baleen whales, shift towards cold-water, high nutrient plankton assemblages at high latitude, expansion of terrestrial mammals) major tectonic events (e.g., opening of Southern Hemisphere Oceanic gateways, shift to the 4-layer structure of the modern ocean, collision of the African-Arabian-Eurasian plates, uplift of the Alpine and Himalayan mountain belt) and global climate forcing (e.g., change from greenhouse to icehouse conditions) (Cerling, 1997; Houben et al., 2013; Norris et al., 2013; Cermeño et al., 2015; Mutz et al., 2018; Komar and Zeebe, 2021). The acceleration of Cenozoic climate cooling started after the Early Eocene Climatic Optimum (EECO; ~52-50 Ma), with temperatures ~10-12 °C warmer than the modern deep ocean, followed by the appearance and expansion of the Antarctic ice-sheets after the Eocene-Oligocene Transition (EOT; ~34 Ma) and ultimately culminating in the extensive Northern Hemisphere glaciation of the Pleistocene (~2.6-0.01 Ma; Zachos et al., 2001; Lear et al., 2008; Mudelsee et al., 2014; Abdullayev et al., 2021). This long-term transition in Earth`s climate is well documented in marine sedimentary archives, but its impact on the evolution of continental ecosystems remains poorly constrained, mainly because continuous, well preserved terrestrial records are scarce and the responses to climate change in these settings are highly complex, depending on latitude, proximity to coast and mountain ranges, position relative to climatic winds, vegetation etc. (e.g., Caves Rugenstein and Chamberlain, 2018; Baldermann et al., 2020). An exception is the sedimentary archive of the Valley of Lakes (Mongolia), which hosts a ~34-21 Ma record of continental sedimentation in Central Asia. The biostratigraphy and the correlation between different outcrops in this basin are well established based on mammalian communities and gastropod records (Harzhauser et al., 2017), magnetostratigraphy (Sun and Windley, 2015) and radiometric age dating of different basalt horizons (Daxner-Höck et al., 2017), rendering this

locality suitable for constraining the links between tectonism and climate change in Central

Asia during the Cenozoic. The Eocene to Miocene of Central Asia was characterized by

accelerated aridification (Dupont-Nivet et al., 2007; Xiao et al., 2010; Bosboom et al., 2014;

Li et al., 2016), expressed as a substantially expanded Gobi Desert relative to today (Guo et

al., 2008; Lu et al., 2019) and a sudden turnover in the mammal record (Harzhauser et al., 2016;

Barbolini et al., 2020). Several, partially opposing hypotheses have been proposed to explain

the aridification of Central Asia, including a combination of orbitally-driven climate forcing,

the stepwise retreat of the proto-Paratethys Sea and uplift of the Tibetan Plateau (Pälike et al.,

2006; Zhongshi et al., 2007; Li et al., 2020) or a continuous decrease of moisture transport by

the westerlies due to exhumation of the Tian Shan and Altai mountains (Caves et al., 2014;

Caves et al., 2015; Caves Rugenstein and Chamberlain, 2018). However, the evolution of

Central Asia`s hydroclimate in the Cenozoic was not a period of continuous aridification;

indeed, the climatic conditions in particular in the Oligocene were highly complex and

characterized by numerous glacial-interglacial cycles (Xiao et al., 2010). Recently, Richoz et

al. (2017) have identified two aridification pulses in Central Asia, in the early and late

Oligocene, which they assigned to global climatic events. To date, a correlation of the global

marine record with the terrestrial record of Mongolia is barely developed (Harzhauser et al.,

2016; Harzhauser et al., 2017; Richoz et al., 2017), which limits our understanding of the

relative influences of climate change and regional tectonics on the evolution of hydroclimate

and weathering conditions in Central Asia in the Cenozoic.

In this contribution, we greatly extend the existing mineralogical and (isotope) geochemical

dataset previously reported in Richoz et al. (2017) for the Eocene-Miocene sediments from the

Valley of Lakes (Mongolia): K-Ar ages and polytype analysis of detrital and authigenic illitic

phases coupled with discrimination function analysis and sedimentological-petrographical-

geochemical inspection are used to constrain provenance, palaeo-environmental conditions and

102 post-depositional alteration history of this sedimentary succession. Systematic, coherent

103 changes in the weathering patterns of silicate detritus and pristine $\delta^{18}O$ and $\delta^{13}C$ signatures

104 recorded in paleosols carbonates allow us to revise and refine the evolution of hydroclimate

105 and weathering conditions in Central Asia in the Cenozoic.

106

107 **2. Geological framework**

108 The Valley of Lakes is an ESE-WNW striking sedimentary basin with ~500 km extension in

109 largest dimension. It is located in Central Mongolia and bordered by the Khangai mountains in

110 the north and the Gobi Altai mountains in the south (Fig. 1a). The geological super-units in the

111 north of Mongolia contain Neoarchean, Proterozoic and Palaeozoic rocks of the Caledonian

112 orogen as well as late Neoproterozoic to Ordovician (Tuva-Mongol) magmatic arc and related

113 back- and fore-arc intrusions, accretionary wedge sequences and ophiolites (Porter, 2016). The

114 geological super-units in the south are characterized mainly by a Palaeozoic orogen, especially

115 the Kazakh-Mongol magmatic arc, which forms the border between Mongolia and China.

116 These units include mainly Devonian to Carboniferous island arc volcanic rocks, Ordovician

117 to Silurian volcanics, Ordovician to Carboniferous metamorphosed sedimentary sequences and

118 Permo-Carboniferous granitoids (Porter, 2016).

119 Regarding the regional lithostratigraphic context, the northern structural units of the Valley of

120 Lakes basin in the Taastsiin Gol area comprise dominantly fault- and thrust-bounded crystalline

121 basement of Neoarchean to Palaeozoic age (Fig. 1b). These include the Baidrag (high-grade

122 gneisses, charnockites and amphibolites, up to 2.65 Ga old) and the Burdgol zone (metapelites,

123 metapsammites and metacherts, 699 ± 35 Ma) in its southernmost end (Teraoka et al., 1996).

124 Further structural units towards the north are the Bayan Khongor (metamorphosed basic rocks,

125 ophiolites and pelitic schists, 450 Ma), the Dzag (metapelites and metapsammites, 440 ± 22

126 Ma and 395 ± 20 Ma) and the Khangai zone (unmetamorphosed, but tectonically deformed

sandstones, mudstones and intercalated olistolith sequences of unspecified Devonian to Carboniferous age) (Teraoka et al., 1996; Höck et al., 1999). All of these zones are intruded by numerous granitoids of variable age (Proterozoic to Cretaceous) and composition (Höck et al., 1999). The major zones located in the south of the Valley of Lakes basin comprise the Baga Bogd, the Ikh Bogd and the Bogd som, which are petrographically indistinguishable from the time-equivalent metasediments and metavolcanics of the Bayan Khongor zone and of the Permian quartzitic conglomerates from the adjacent Mount Ushgoeg (Höck et al., 1999).

In the focus of this study are the fossiliferous siliciclastic sediments of the Taatsiin Gol Basin, which record important information about changes in sediment provenance, weathering paths and conditions and palaeo-climate in Central Asia during the Eocene to Miocene. The herein investigated sedimentary sections span the Tsagaan Ovoo Formation (upper Eocene), the Hsanda Gol Formation (Oligocene) and the Loh Formation (lower Miocene). Five sections, namely Taatsiin Gol right (TGR-AB), Taatsiin Gol south (TGR-C), Hsanda Gol (SHG-D), Tatal Gol (TAT-E) and Hotuliin Teeg (HTE), were chosen for this study, because of the well-constrained chronological framework at these localities. Based on previous radiometric and magnetostratigraphic dating of these sections (Höck et al., 1999; Sun and Windley, 2015), Harzhauser et al. (2017) have established a precise biozonation of the studied sedimentary succession, which includes, from the bottom to the top, Zone A (early Rupelian: 33.9 Ma to ~31.5 Ma), Zone B (late Rupelian: ~31.5 Ma to ~28.1 Ma), Zone C (early Chattian: ~28.1 Ma to ~25.6 Ma), Zone C1 (mid-Chattian: ~25.6 Ma to ~24.0 Ma), Zone C1-D (late Chattian ~24.0 Ma to ~23.0 Ma) and Zone D (Aquitanian: ~23.0 Ma to ~21.0 Ma).

These sections form an integrated sedimentary succession with a thickness of ~115 m (Richoz et al., 2017). Two prominent stratigraphic marker beds, the basalt I group (32.4-29.1 Ma) and the basalt II group (28.7-24.9 Ma) crop out at ~40-41 m and at ~94-100 m in the sedimentary profile (Daxner-Höck et al., 2017). A younger basalt III group (13.2–12.2 Ma) dates back to

152 the middle Miocene, but is not part of the sedimentary succession investigated here. Further

153 details about the local nomenclature, the investigated profiles, profile correlation and

154 lithostratigraphic relationships are provided in Harzhauser et al. (2017), Daxner-Höck et al.

155 (2017) and Richoz et al. (2017). Due to the complex architecture of the Valley of Lakes basin

156 and adjacent areas, a mixed provenance has been proposed for the basin fill, however, detailed

157 knowledge about the palaeo-depositional environment and source area relationships remain

158 poorly constrained (Höck et al., 1999).

159

160 **3. Materials and Methods**

161 3.1 Materials

162 Representative bulk sediment samples (140 in total) were taken from different outcrops, which

163 cover the entire sedimentary succession of the Valley of Lakes from the upper Eocene to the

164 lower Miocene. The layers sampled vary in color, composition, texture, fossil and carbonate

165 content, etc., however, they do not show optical signs of alteration, such as recent surface

166 weathering. Samples for geochemical, isotopic and mineralogical analysis were crushed in a

167 ball mill for 10 min and micronized using a McCrone mill for 8 min, with ethanol addition.

168 Samples with a high clay mineral content based on an initial mineralogical inspection were

169 selected further for an identification of the clay mineral suite, which is defined here as $< 2\ \mu m$

170 size fraction (Rafiei et al., 2020). As for the clay mineral separation, 5 g of the bulk material

171 was reacted with 5 % HCl for 10 min to remove the carbonates, followed by standard Atterberg

172 sedimentation and subsequent collection and drying of the $< 2\ \mu m$ size fraction at 40 °C. Fast

173 acid digestion was used to reduce leaching or dissolution of the clay minerals under acidic

174 conditions (Baldermann et al., 2012). Four samples from the Hsanda Gol Formation with a

175 high amount of illitic phases were used for an illite polytype and K-Ar analysis. To this end,

176 three sub-fractions (< 1 µm, 1-2 µm and 2-10 µm) were separated by Atterberg sedimentation,

177 which all represent mixtures of authigenic illitic phases and detrital illite/muscovite.

178

179 3.2 Analytical methods

180 The major, minor and trace element composition of a sub-set of samples (91 in total) was

181 analyzed via a Philips PW2404 wavelength dispersive X-ray fluorescence (XRF) spectrometer.

182 Fine powdered samples (0.8 g) were heated to 1050 °C to remove the volatile components

183 (CO_2, H_2O, etc.), following determination of the loss on ignition (LOI) by gravimetric analysis.

184 The residuals were fused at 1200 °C using $LiBO_2$ (4 g) as the fluent agent. The standard glass

185 tablets were analyzed together with a set of USGS standards (analytical error: ± 0.5 wt% for

186 the major elements; Richoz et al., 2017).

187 Sediment origin and variations in the detrital influx among the different provenance areas were

188 depicted using discrimination plots calculated on the basis of major oxide compositions (Roser

189 and Korsch, 1988). The weathering paths and intensities in the source rock areas were assessed

190 through changes in the weathering indices, such as the chemical index of alteration (CIA), the

191 chemical index of weathering (CIW) and the plagioclase index of alteration (PIA), which were

192 calculated based on the major oxide compositions using the following equations (Nesbitt and

193 Young, 1982; Abdullayev et al., 2021):

194 $CIA = (Al_2O_3 / (Al_2O_3 + CaO^* + Na_2O + K_2O)) \times 100$

195 $CIW = (Al_2O_3 / (Al_2O_3 + CaO^* + Na_2O)) \times 100$

196 $PIA = (Al_2O_3 - K_2O) / (Al_2O_3 + CaO^* + Na_2O - K_2O) \times 100$,

197 where CaO^* denotes the fraction of CaO present in the silicate fraction. CaO^* was calculated

198 by subtraction of the total CaO content of the bulk sediments (determined by XRF analyses)

199 from the CaO content associated with carbonate minerals (determined by XRD analyses, see

below). The weathering conditions of the source areas were identified further using Al_2O_3 –

$CaO^* + Na_2O – K_2O$ (A-CN-K) ternary diagrams (Nesbitt and Young, 1984).

The mineralogical composition of all bulk samples was determined by Rietveld-based analysis of X-ray diffraction (XRD) patterns recorded on a PANalytical X'Pert PRO diffractometer (Co-Kα; 40 kV and 40 mA) equipped with a high-speed Scientific X'Celerator detector. The top loading technique was used for the preparation of randomly oriented samples, which were examined in the range from 4-85 2θ with 0.008°2θ/s step size and 40 s count time. The PANanalytical X`Pert Highscore Plus software and a pdf-4 database were used for mineral quantification (analytical error: < 3 wt%; Baldermann et al., 2021). The separated grain size sub-fractions were X-rayed under identical operational conditions. The amounts of authigenic (1M and $1M_d$ polytype) and detrital ($2M_1$ polytype) illitic phases were calculated using the following equations (Grathoff and Moore, 1996):

$\%2M_1 = 2.05 + 360 \times A_{(114)}/A_{(2.6\ Å\ band)}$

$\%1M = 4.98 + 136 \times A_{(-112)}/A_{(2.6\ Å\ band)}$

$\%1\ M_d = 100 − \%1M\ or\ 100 − \%2M_1$

where A is the area (in cps·2θ) of the polytype-specific hkl-reflections of illite and of the 2.6 Å band, respectively (analytical error: ~± 5 %; Baldermann et al., 2017).

Oriented clay films were prepared for the further characterization of the clay mineral fraction (< 2 μm) using a Phillips PW 1830 diffractometer (Cu-Kα; 40 kV and 30 mA) outfitted with a graphite monochromator and a scintillation counter. The clay films were prepared by mixing 50 mg of clay fraction with 5 mL of deionized water, following ultrasonic treatment in a water bath for 10 min to produce a clay-in-suspension, which was subsequently sucked through a porous ceramic tile of ~4 cm² size (Baldermann et al., 2014). The clay films were examined in the range from 3-30° 2θ with 0.02° 2θ step size and 2 s/step count time, each at air-dry states, after solvation with ethylene glycol (EG) and after heat treatment at 550 °C for 1 h. The

proportion of illite layers (%Ilt) in mixed-layered illite-smectite (Ilt-Smc) was calculated based on the position of the 002-reflections obtained from XRD patterns of EG-solvated clay films (d_{EG-002} in Å) following the equation (analytical precision: ± 5 %; Baldermann et al., 2017):

$$\%\,Ilt = 60.8 \times d_{EG-002} - 504.5.$$

Illite crystallization ages were calculated through coupled illite polytype and K-Ar analysis carried out on the separated grain size sub-fractions. The K_2O content of these samples was determined in digested aliquots (1M HF and HNO_3 mixture) in duplicate via a BWB-XP flame photometer™ using 1 % CsCl as the ionization buffer and 5 % LiCl as the internal standard. The Ar isotopic composition was analyzed in a stainless-steel extraction and purification line connected to a Thermo Scientific ARGUS VI™ noble gas mass spectrometer operated in static mode at the University of Göttingen (Germany). The radiogenic ^{40}Ar content was measured using the standard isotope dilution method applying a highly enriched ^{38}Ar spike calibrated against the biotite standard HD-B1. K-Ar age calculations were made based on the constants recommended by the IUGS (for details see Wemmer et al., 2011). The grain size sub-fractions are free of K-containing mineral phases other than mica/illite group minerals, which would disturb the radiogenic K-Ar ages.

A scanning electron microscopy (SEM) study was carried out to characterize the mineralogy, chemical composition, microfabrics and alteration patterns of the authigenic and detrital (clay) minerals present in the sediments. Therefore, specimens were prepared on standard SEM stubs, coated with carbon and analyzed using a GEMINI® Zeiss Ultra 55 microscope operated at 5-15 kV of accelerating voltage and equipped with a high efficiency in-lens secondary electron (SE) detector and an EDAX Si(Li)-detector for high-resolution imaging and energy-dispersive X-ray spectrometry (EDX) analysis.

The $\delta^{13}C$ and $\delta^{18}O$ isotopic composition of the carbonate fraction was analyzed to constrain the palaeo-climatic trends recorded in the paleosols. In a previous study (Richoz et al., 2017) it

was shown that the soil carbonates (calcrete nodules, lenses and crusts) mostly record pristine $\delta^{13}C$ and $\delta^{18}O$ isotopic compositions reflective of conditions during their formation and are not influenced by detrital or secondary carbonates, such as calcite spar or dolomite. The samples (139 in total) were reacted with 102 % phosphoric acid at 70 °C in a Kiel II automated reaction system and the liberated CO_2 gas analyzed with a ThermoFinnigan mass spectrometer MAT Delta. The measured $\delta^{13}C$ and $\delta^{18}O$ values were corrected against the NBS19 standard and are reported in per mill (‰) relative to the Vienna-PeeDee Belemnite (V-PDB) standard (analytical precision: < 0.05 ‰ for $\delta^{13}C$ and < 0.1 ‰ for $\delta^{18}O$; Richoz et al., 2017).

4. Results

4.1 Sediment petrography

An integrated lithostratigraphic profile of the investigated sedimentary succession (upper Eocene to lower Miocene) from the Taatsiin Gol region, which is a part of the Valley of Lakes, including the biozonation and some field impressions, is presented in Figure 2.

The sediments from the Tsagaan Ovoo Formation (upper Eocene) are dominantly coarse clastic sand and gravel deposits of white-greyish color with embedded clay and silt layers of greyish-yellow-green to reddish-brown color, depending on the Fe content (Richoz et al., 2017). The coarser beds show cross-bedding and are frequently poorly sorted, while the finer layers show trough and planar cross-bedding, lamination, inverse to normal grading, rarely ripples and channel fills, and are better sorted. Roots and plant debris and bioturbation features, such as burrows, indicate local paleosol formation (Richoz et al., 2017).

The overlying Hsanda Gol Formation (Oligocene) has a higher fossil content (mainly remains of small mammals) and appears as horizontally bedded and poorly sorted clay to silt layers of brick-red to reddish-brown color with intercalated cross-bedded sandstone beds and minor sand and granule lenses of greyish color (Fig. 2c). Paleosol formation is documented by abundant

275 crypto- to microcrystalline calcite nodules and calcite crusts of centimeter to decimeter size

276 encapsulating soil and plant materials (Fig. 2b; Richoz et al., 2017). These calcrete layers of

277 greyish-white color are partially intergrown with Fe- and Mn-(oxy)hydroxides of orange-

278 greyish-black color. The basalt I and basalt II horizons are exposed at ~40-41 m and at ~94-

279 100 m and interfinger with the sediments from the Hsanda Gol Formation (Fig. 2b,d).

280 The Loh Formation (lower Miocene) comprises generally poorly sorted and structure-less silty-

281 clayey horizons with embedded pebbles and lenses of greyish-white to reddish-brown color as

282 well as trough to planar cross-bedded sand and gravel beds of greenish-yellow-red color, which

283 are deposited in alternate mode. Sedimentary structures seen in the coarser beds include inverse

284 to normal grading, ripple marks, channel and scour fills and overbank fines (Richoz et al.,

285 2017). Most horizons are highly fossiliferous (remains of small mammals and gastropods) and

286 show signs of paleosol formation, such as calcite nodules and crusts incorporating plant debris,

287 and burrow structures (Harzhauser et al., 2017).

288

289 4.2 Bulk and clay mineralogy

290 The mineralogical composition of the Valley of Lakes samples is dominated by quartz (10-55

291 wt%), illite/muscovite (10-50 wt%), calcite (0-70 wt%), feldspar (5-15 wt%; mainly albite and

292 plagioclase and minor orthoclase) and hematite (0-10 wt%) (Table S1). XRD analysis identifies

293 the illite/muscovite as an almost pure illitic phase composed of > 95 % Ilt layers and < 5 %

294 Smc layers (Fig. S1) with the $1M_d$ polytype structure dominating (~90-95 % of the total illite

295 fraction; Fig. S2). The proportions of the 1M and $2M_1$ polytype structures of illite do not exceed

296 ~5-10 % of the total illite fraction. Kaolinite, chlorite (Mg-rich), mixed-layered Ilt-Smc

297 comprised of ~30-10 % Ilt layers and ~70-90 % Smc layers (Fig. S1) as well as Ti-oxides (rutile

298 and anatase) represent minor constituents (Fig. S2), accounting altogether for less than ~5 wt%

299 of the sediments. Trace amounts of zeolite and amphibole (< 5 wt%) are documented between

12

300   ~35 and 45 m and between ~90 and 110 m in the sedimentary succession, i.e., adjacent to the

301   basalt I and II groups. Vermiculite, dolomite, ankerite, anhydrite, halite and pyrite were not

302   identified in the samples, which contrasts observations made by Höck et al. (1999).

303   The sediments from the Tsagaan Ovoo Formation have the highest proportions of quartz, illite,

304   feldspar and hematite and the lowest content of calcite compared to the other two formations,

305   consistent with less abundant calcrete horizons developed in the upper Eocene sediments (Fig.

306   3a). The sediments from the Oligocene Hsanda Gol and lower Miocene Loh formations have

307   highly variable, but on average higher calcite contents than the Tsagaan Ovoo Formation due

308   to abundant paleosol formation and related lower contents of silicate minerals and hematite

309   (Fig. 3b,c). The depletion of hematite in these samples argues for a detrital origin and for the

310   precipitation of this mineral phase on silicate detritus during sediment transportation under oxic

311   conditions. No systematic trends in the abundance of the mineral phases was observed across

312   the investigated profile (cf. Table S1).

313

314   4.3 Microfabrics and illite crystallization ages

315   A microstructural study of weakly consolidated samples taken from the Hsanda Gol Formation

316   reveals (sub)angular to rounded detrital quartz grains (Fig. S3a), which are partly overgrown

317   by diagenetic quartz cement (Fig. S3b), as well as partially dissolved feldspar grains (Fig. S3c).

318   Calichized areas are cemented by calcite spar, which appears as crypto- to microcrystalline

319   material with aggregate particle sizes in the micrometer to millimeter range (Fig. S3d). All

320   these components are covered or intergrown by fine hematite particles (Fig. S3e), although silt-

321   size hematite grains are also observable. Coarse chlorite flakes as well as tiny, rounded to

322   vermiform kaolinite particles are barely seen (Fig. S3f). Indeed, the clay mineral suite is

323   dominated by two types of illite and one type of Ilt-Smc. SEM-EDX analysis suggests the illites

324   have higher contents of Al_2O_3 and K_2O, but lower contents of SiO_2 and Na_2O than the Ilt-Smc.

13

325 The illites occur either as micrometer-sized particles with platy or pseudohexagonal forms

326 being evenly dispersed throughout the matrix (type 1: Fig. 4a,c,e,g) or as long (micrometer-

327 scale), but thin laths and fibers, which grow into the open pore space (type 2: Fig. 4b,d,f,g,h).

328 The latter type of illite is often referred to as "hairy illite" (Güven et al., 1980; Rafiei et al.,

329 2020). The Ilt-Smc is a nanometer-sized material with flaky to irregular particle forms, which

330 covers detrital grains or grows into the open pore space (type 3: Fig. 4b,d,h).

331 When viewed together with the results of the illite polytype analysis and measured K-Ar ages

332 (Table 1), all sub-samples represent physical mixtures of detrital $2M_1$ illite/muscovite (type 1),

333 authigenic $1M_d$/1M illite (type 2) and authigenic $1M_d$ Ilt-Smc (type 3). Accordingly, the plot

334 of the proportion of $2M_1$ illite/muscovite against the K-Ar age of a given sub-sample (Fig. 5)

335 provides individual crystallization ages for the detrital and authigenic illitic phases (Grathoff

336 and Moore, 1996): The upper intercept of the best-fitting line at 100 % of $2M_1$ reveals the

337 crystallization age of detrital illite/muscovite, which is 727.6 to 797.9 Ma. The lower intercept

338 of the best-fitting lines at 100 % of $1M_d$ + 1M gives crystallization ages for the authigenic clay

339 minerals, which vary between 25.2 and 34.2 Ma.

340

341 4.4 Geochemistry and weathering indices

342 Variations in the major element composition of the samples (Table S2) follow changes in the

343 abundance of silicate minerals (e.g., quartz, feldspar and clay minerals) relative to calcite and

344 hematite across the sedimentary succession. No distinct trends among the different formations

345 are seen, except for a lower CaO content and higher contents of SiO_2, Al_2O_3, K_2O, Na_2O, MgO

346 and Fe_2O_3, on average, in the Tsagaan Ovoo Formation, compared to the Hsanda Gol and Loh

347 formations, corroborating the mineralogical and petrographic results (cf. Table S1 and Fig. 3).

348 Minor amounts of TiO_2 belong to rutile and anatase and traces of MnO and P_2O_5 correspond

349 to Mn-oxides and apatite. The positive correlations of Cu, Ga, Rb and Zn with Al_2O_3 as well

as Ce, La, Y and Zr with TiO_2 and Sr with CaO point to their association with clay minerals

(i.e., structural incorporation or sorption onto the clay mineral surface), heavy minerals and

carbonate minerals, respectively (Abdullayev et al., 2021). Ba, Co, Cr, Hf, Nb, Ni, Pb, Sc, Th,

V and U are inconspicuous due to lack of correlation with Al_2O_3 and TiO_2 or low concentration

in the samples.

The plot of the chemical data in the A-CN-K ternary diagram (Fig. 6) shows the samples fall

within or plot slightly above the compositional range of Post-Archean Australian Shale (PAAS)

and Average Proterozoic Shale (APS) and thus follow the predicted weathering trend for basalt

protoliths and Upper Continental Crust (UCC) rocks (Nesbitt and Young, 1984; Bahlburg and

Dobrzinski, 2011). The shift of most of the data toward the K pole of the diagrams indicates

K-metasomatism has affected the chemical composition of the sediments through the growth

of authigenic illite and Ilt-Smc (Fedo et al., 1995), consistent with petrographic observations

and clay polytype analyses. The CIA, CIW and PIA values vary from 70-83, 83-97 and 79-96

across the different formations, which averages of 79, 94 and 92 for the Loh Formation and 76,

90 and 88 for both the Hsanda Gol and Tsagaan Ovoo formations, respectively (Table S3).

4.5 Soil carbonate $\delta^{18}O$ and $\delta^{13}C$ isotopic composition

The $\delta^{18}O$ and $\delta^{13}C$ values of the soil carbonates vary in the range from -11.7 to -0.2 ‰ and -

8.1 to -3.8 ‰ across the sedimentary succession of the Valley of Lakes (Table S4). Six samples

taken close to the basalt I and II groups show comparatively lighter isotope values, -12.9 to -

8.6 ‰ of $\delta^{18}O$ and -9.4 to -8.3 ‰ of $\delta^{13}C$, which indicates post-depositional overprinting.

Therefore, these samples are not considered further. A high scatter in $\delta^{18}O$ values (-9.3 to -0.2

‰) and relatively light $\delta^{13}C$ values (-7.5 to -6.4 ‰) are seen in the lower part of the Hsanda

Gol Formation, changing into less fluctuating $\delta^{18}O$ values (-10.3 to -7.0 ‰) and systematically

heavier $\delta^{13}C$ values (-7.6 to -3.8 ‰) in the middle and upper part of the Hsanda Gol Formation

375 until the lower Miocene. Around the series/stage boundary, a gradual shift towards lighter $\delta^{18}O$

376 values (-11.7 to -8.6 ‰) and fluctuating, but lighter $\delta^{13}C$ values (-8.1 to -4.4 ‰) are evident.

377

378 **5. Discussion**

379 5.1 Sediment provenance

380 The time interval from the Neoarchean to the late Permian saw the development of large parts

381 of the fault- and thrust-bounded crystalline basement of Mongolia. The main lithological units

382 forming this basement include Neoarchean metamorphic rocks and Palaeozoic metasediments

383 and magmatic rocks, which are all intruded by volcanic and magmatic rocks of various age,

384 composition and provenance (Zorin et al., 1993). This complex architecture and the denudation

385 processes in the Mesozoic, which formed the Valley of Lakes basin and created the present-

386 day regional landscape and relief, are documented in the heavy mineral spectra of the Cenozoic

387 basin fill (Höck et al., 1999): the presence of epidote, amphibole, garnet, rutile, pyroxene,

388 sphene, zircon and tourmaline suggest that a mountainous region in the area of the present-day

389 Khangai mountains were the potential source areas (McLennan et al., 1993). Quartz, pegmatite,

390 granite, siltstone, basalt and carbonate clasts found in the gravel fraction (Höck et al., 1999)

391 are also indicative of a heterogeneous provenance for the Valley of Lakes sediments.

392 The major oxide compositions of the sediments from the Valley of Lakes mainly plot in the

393 "P4-quartzose sedimentary provenance" field and only a few samples plot into the "P1-mafic

394 igneous provenance" field in the Roser and Korsch (1988) discrimination diagram (Fig. 7).

395 This indicates metamorphosed sediments rich in quartz and poor in feldspar and subordinate

396 mafic to intermediate igneous and metamorphic rocks are the source rocks for the Valley of

397 Lakes sediments. These rock types are common to all lithological units exposed in the adjacent

398 lands of the Valley of Lakes (Höck et al., 1999). However, if considering the crystallization

399 ages of the $2M_1$ detrital illite/muscovite (727.6 to 797.9 Ma, cf. Fig. 5), a robust assignment to

16

400 provenance areas in the adjacent northern Burdgol zone and Baidrag zone is possible. The

401 Burdgol zone hosts dominantly metapelites, metapsammites and metacherts, which have an

402 age of 699 ± 35 Ma, as inferred from K-Ar dating of muscovite (Teraoka et al., 1996), which

403 closely matches the detrital illite/muscovite ages measured in the sediments from the Valley of

404 Lakes. The shift towards older ages can be explained by a minor contribution of Neoarchean

405 rocks from the nearby Baidrag zone (~2.65 Ga old), which are comprised of high-grade

406 gneisses, charnockites and amphibolites. Both source areas coincide with the heavy mineral

407 spectra and gravel lithologies of the Valley of Lakes sediments (Höck et al., 1999).

408 Assuming the detrital illite/muscovite in the Valley of Lakes sediments is a mixture of eroded,

409 metamorphosed and/or intruded material from both source regions, a relative contribution of

410 ~> 95 % from the Burdgol zone and~< 5 % from the Baidrag zone to the total detrital mica

411 fraction can be calculated. Detrital silicate influx from the northernmost Bayan Khongor zone,

412 Dzag zone and Khangai zone is considered to be unlikely, as these source areas are geologically

413 younger (Ordovician to Cretaceous) (Teraoka et al., 1996). Mixtures of different proportions

414 of detritus from the Burdgol zone and some younger and older material are unlikely as well, as

415 constant source proportions over time would be required to explain the same ages for the four

416 investigated samples. This assertion is consistent with the conclusion drawn by Richoz et al.

417 (2017), who have argued that the overall sedimentation system and the sediment provenance

418 areas have not significantly changed in the considered timeframe. Therefore, the source area

419 relationships of the sediments from the Valley of Lakes are less complex than previously

420 thought with most detritus delivered from the regionally adjacent northern areas located within

421 a 100 km range. Thus, variation in the chemical weathering indices outlined below most likely

422 record changes in the weathering conditions of the source rock areas rather than changes in the

423 sedimentary facies at the same time.

424

5.2 Depositional environment

The poorly sorted, massive to partly cross-bedded sand and gravel beds of the Tsagaan Ovoo Formation are interpreted as debris flow deposits in alluvial fans, according to the classification of Miall (1996) for fluvial sediments. These were generated during or soon after heavy rainfall events, which caused the water-saturated regolith to move down slope (Hubert and Filipov, 1989). The finer, laminated layers with ripple marks, inverse to normal grading and channel fills deposited in-between the coarser clastic beds represent the background sedimentation in the upper Eocene, i.e., braided river deposits developed in close vicinity to propagating alluvial fans (Miall, 1996). Imbrications of pebbles, cobbles and clasts within these beds suggest a palaeo-current direction from north to south (Höck et al. 1999), which is consistent with major sediment source areas in the northern Burdgol Zone. In contrast to Badamgarav (1993) and Daxner-Höck et al. (2017), we found no petrographic-sedimentological evidence for lake or playa sedimentation in the upper Eocene strata, which we attribute to the different sample types considered: While Badamgarav (1993) and Daxner-Höck et al. (2017) identified efflorescent salt crusts composed of halite, tepees and polygonal structures in some sedimentary layers, no such structures were observed in the paleosol horizons of the same age. However, the scatter in the $\delta^{18}O$ isotopic composition of the soil carbonates, which has been attributed to varying amounts of evaporation (Richoz et al., 2017), is consistent with a playa lake setting.

The poorly sorted, often horizontally bedded and fossiliferous clay-silt-sand(stone) beds of the Hsanda Gol Formation were deposited in a complex environment: the finer beds have likely been developed in ephemeral lakes or braided rivers systems draining proximal alluvial fans, as indicated by the presence of channel sand bodies with basal channel scour lags and cross-bedded sand fill. The sandier beds are interpreted as open steppe deposits, which have been temporarily affected by ephemeral river and playa lake sedimentation (Miall, 1996), as it can be inferred from occasional mud cracks and salt crusts (halite; Höck et al., 1999). On the

450   contrary, Sun and Windley (2015) have proposed an eolian origin for the Oligocene sediments

451   and interpreted them as loess deposits, which were transported by westerly winds, based on

452   REE patterns and comparison with grain size distributions obtained from recent Loess deposits

453   from Kansas (USA) and the Chinese Loess Plateau. Although we cannot exclude long-distance

454   transport and subsequent deposition of dust has contributed to at least a minor proportion to

455   the total basin fill of the Valley of Lakes, we found no petrographic evidence for any aeolian

456   influences, such as ripples, coarsening up laminae or climbing translatent strata, ventifacts,

457   mud curls or even quartz grains with crescentic percussion marks (Kenig, 2006; Li et al., 2020).

458   The lithological variability of the Loh Formation (i.e., poorly sorted and highly fossiliferous

459   clay-silt-sand-gravel beds deposited in alternate mode) can be best explained by a combination

460   of debris flow deposits in alluvial fans (coarse clastic material) and abandoned channel deposits

461   and waning flood sedimentation (fine clastic material) of a shallow, perennial flowing braided

462   river system Miall (1996). Imbrication of gravels and flow structures in the basalt III group still

463   indicate a palaeo-current direction from north to south (Höck et al., 1999), which suggests the

464   Burdgol Zone is the main source area at least up to the upper lower Miocene.

465

466   5.3 Origin of hairy illite and Ilt-Smc

467   Höck et al. (1999) and Sun and Windley (2015) have proposed an aeolian origin or a coupled

468   aeolian-fluviatile origin for the finest fraction of the Valley of Lakes sediments, while Richoz

469   et al. (2017) concluded the finest fraction is authigenic and has been formed during or shortly

470   after the flows of the different basalt groups. However, in none of the above studies radiometric

471   ages of the clay fraction have been presented to confirm their assertions. Our XRD and SEM

472   study shows the clay mineral fraction of the Oligocene Hsanda Gol Formation is dominated by

473   hairy illite and subordinate flake-shaped Ilt-Smc, which cover detrital grains or grow into the

474   pore space (Fig. 4). All these features that are typical for authigenic illitic phases (Güven et al.,

19

475   1980; Rafiei et al., 2020). The polytype analysis and K-Ar age dating reveal these illitic phases

476   have been precipitated between 34.2 and 25.2 Ma (Fig. 5), which (within uncertainty of the K-

477   Ar age dating method we have used here) is well within the documented intrusion ages of the

478   basalt I group (32.4-29.1 Ma) and basalt II group (28.7-24.9 Ma) (Daxner-Höck et al., 2017)

479   and closely matches the biozonation reported in Harzhauser et al. (2017).

480   The origin of Ilt-Smc in the Valley of Lakes sediments is difficult to constrain: it could have

481   been formed during low temperature pedogenesis from smectite or kaolinite precursors of

482   'zero' age (Huggett et al., 2016), which were deposited due to wind (allochthonous clay source)

483   or soil water (autochthonous source) action, through a dissolution-(re)precipitation mechanism.

484   Pedogenic degradation of detrital illitic minerals to produce Ilt-Smc under acidic conditions at

485   low temperature has also been observed (Meenakshi et al., 2020). Contrary, several published

486   studies question a low temperature origin of Ilt-Smc in sedimentary successions: Ilt-Smc found

487   in paleosols from the Illinois Basin was shown to be the alteration product of siliceous parental

488   phases, which interacted with hydrothermal brines generated during burial diagenesis rather

489   than of ancient soil formation processes (McIntosh et al., 2020). Środoń (1984) concluded that

490   smectite and Ilt-Smc phases are relatively stable in surface-near surroundings until the elevated

491   temperatures of deep diagenesis are reached, which is consistent with slow kinetics of smectite

492   illitization calculated for shallow buried sediments and/or low temperature settings (Cuadros,

493   2006). In the case of the Valley of Lakes sediments, the relatively low Ilt content in Ilt-Smc

494   (~10-30 % Ilt layers) and the stratigraphic age-progression of the authigenic illitic phases up-

495   section in the sedimentary succession may indicate a pedogenic origin of the Ilt-Smc.

496   Contrary to the Ilt-Smc, a pedogenic origin of the hairy illite is unlikely, because the formation

497   of this mineral phase requires temperatures well around 100 °C (Güven et al., 1980; Nadeau et

498   al. 1985; Baldermann et al., 2017), which is unrealistic high to occur in a developing soil profile

499   that has experienced a maximum burial depth of only a few hundred meters (Richoz et al.,

500   2017). The high Ilt content (> 95 % Ilt layers) and the hairy appearance of the illite argue for a

501   formation at elevated temperatures, which likely developed simultaneously or shortly after the

502   prominent and recurrent basalt flows, consistent with a basalt-mediated diagenesis. Under such

503   conditions, pore fluids rich in K^+, Al^{3+} and silicic acid are generated through the dissolution of

504   unstable components, such as feldspar, which subsequently infiltrated the poorly consolidated

505   (porous) Valley of Lakes sediments, thereby promoting the direct precipitation and growth of

506   hairy illite in open pores (Fig. 4) and/or the hydrothermal alteration of pre-existing pedogenic

507   Ilt-Scm to hairy illite (Baldermann et al., 2017). This mechanism is applicable to explain the

508   shift of the chemical data towards the K pole in the A-CN-K ternary diagram (Fig. 6).

509

510   5.5. Palaeo-climate and weathering conditions

511   Climatic conditions are a primary control of the intensity and type of terrestrial weathering

512   processes, where humid periods favor chemical weathering and arid periods favor physical

513   weathering (Chamley, 1989). Analogously, hydroclimatic conditions take a key control on the

514   intensity of pedogenic processes, which can be recorded in the $\delta^{13}C$ and $\delta^{18}O$ isotopic signature

515   of authigenic carbonates (i.e., calcrete in paleosols), where wetter conditions favor an excursion

516   towards lighter $\delta^{13}C$ and $\delta^{18}O$ values and drier conditions favor an excursion towards heavier

517    $\delta^{13}C$ and $\delta^{18}O$ values (Richoz et al., 2017). Hence, variations in chemical weathering indicators

518   (CIA, PIA and CIW) and in the $\delta^{13}C$ and $\delta^{18}O$ profiles of soil carbonates across a sedimentary

519   succession can be used to trace and assess fluctuations in the climatic conditions that prevailed

520   in the source areas and in the sedimentary basin at the time of sediment deposition, and during

521   pedogenesis (Nesbitt and Young, 1982; Bahlburg and Dobrzinski, 2011; Fischer-Femal and

522   Bowen, 2020; Kelson et al., 2020; Zamanian et al., 2021). The formation of soil carbonates is

523   a highly complex process that can complicate the interpretation of their $\delta^{13}C$ and $\delta^{18}O$ isotopic

524   values (Richoz et al., 2017), as global climatic trends may be overprinted by regional factors,

525 such as contamination with detrital carbonates, dolomitization, meteoric diagenesis, maturation

526 or oxidation of organic matter, dis-equilibrium conditions between atmospheric (or biogenic)

527 CO_2 and soil solution, evaporation, basalt hydrothermalism, etc. (Kaufman and Knoll, 1995;

528 Kent-Corson et al., 2009; Caves et al., 2014; Li et al., 2016; Baldermann et al., 2020; Li et al.,

529 2020). However, if considering that the pristine soil carbonate $\delta^{13}C$ and $\delta^{18}O$ isotopic signature

530 is almost well preserved in the Valley of Lakes sediments, their use for palaeo-environmental

531 reconstructions is possible.

532 The analysis of the $\delta^{13}C$ and $\delta^{18}O$ isotopic profiles recorded in the soil carbonates from the

533 Valley of Lakes (~34-21 Ma) yielded the following palaeo-climatic trends, which are consistent

534 with inverse shifts seen in the chemical weathering indices (dashed orange lines in Fig. 8), i.e.,

535 periods with increased precipitation coincide with higher chemical weathering indices and vice

536 versa. This inverse relation is a robust recorder of changing humid/arid climatic conditions in

537 an overall arid climate through the Cenozoic in Central Asia, if considering that the source

538 areas providing the silicate detritus have not changed over time in the investigated sedimentary

539 succession and that a stable sedimentation system had been established. Thus, changes in the

540 sedimentary facies, post-diagenetic impacts, basalt flow events or reginal tectonic activities are

541 only barely seen in the soil carbonate $\delta^{13}C$ and $\delta^{18}O$ isotopic profiles. Accordingly, during the

542 late Eocene to the earliest Oligocene comparatively humid to semi-arid climatic conditions

543 prevailed in Central Asia (phase i); biozone A to bottom part of biozone B; ~34-31 Ma), which

544 is followed by an early Oligocene aridification (phase ii); bottom part of biozone B; ~31 Ma)

545 and the establishment of more arid climatic conditions afterwards until the terminal Oligocene

546 (phase iii); upper part of biozone B to biozone C1-D; ~31-23.5 Ma). A shift back towards

547 comparatively humid to semi-arid climatic conditions is evident in the late Oligocene to earliest

548 Miocene (phase iv); transition between biozones C1-D and D; ~23.5-23 Ma), which is followed

549 by the establishment of these conditions in the early Miocene (phase v); biozone D; ~23-21

550 Ma). We note here that the atmospheric CO_2 concentration decreased from 800 ppm to 200

551 ppm from ~33 to 22 Ma (Zhang et al., 2013), which should have shifted the soil carbonate $\delta^{13}C$

552 signatures towards lighter values. However, due to changes in aridification in Central Mongolia

553 at the same time, this trend is not seen in the data. Indeed, an increase in aridification results in

554 a restricted soil moisture content that can i) increase the $\delta^{13}C$ value of soil carbonates, ii) causes

555 the plant productivity to decrease, which affects the ratio of atmospheric CO_2 to soil respired

556 CO_2 and iii) reduce the formation depth of the soil carbonates and thus the relative contributions

557 of atmospheric CO_2 and soil-derived carbon (Cerling and Quade 1993; Caves et al. 2014). As

558 a consequence, the $\delta^{13}C$ isotopic signature of the soil carbonate is linked to aridification pulses,

559 which also affects the weathering intensity of the sediment source areas, explaining the inverse

560 relation between the isotope record and the chemical alteration indices. On the contrary, large

561 changes in the $\delta^{18}O$ isotopic record of pristine soil carbonates are not to be expected given that

562 the hydroclimatic variations are small in the semi-arid setting of the Valley of Lakes and that

563 most moisture is recycled (Caves et al., 2015; Chamberlain et al., 2014; Kukla et al., 2019;

564 Winnick et al., 2014).

565 Global cooling events established from $\delta^{13}C$ and $\delta^{18}O$ isotope records of marine deep-sea

566 sediments (Zachos et al., 2001; Gallagher et al., 2020), such as the Oi-1a/b Glaciation (~34-33

567 Ma) or the Oligocene Glacial Maximum (~28 Ma) are barely recorded in the soil carbonate

568 $\delta^{13}C$ and $\delta^{18}O$ isotope profiles. However, they are visible by increases in chemical weathering

569 indices at exactly these time intervals (blue bars and arrows in Fig. 8) and correspond to

570 important faunal turnovers (Harzhauser et al., 2016). The early Oligocene aridification (~31

571 Ma) is seen by an excursion towards heavier isotopic values between ~55 and 60 m in the rock

572 record, but do not correspond to an important faunal turnover (Harzhauser et al., 2016). On the

573 contrary, the Oligocene warming event (~25 Ma), marked by an important extinction of the

574 mammal community, is not seen in the $\delta^{13}C$ and $\delta^{18}O$ isotopic profiles. However, in the interval

575 from ~87 to 92 m (upper part of biozone C1) an increase of all chemical weathering indices is

576 evident, which we attribute to strong illitization and local overprinting of the pristine chemical

577 signature of these sediments. The following Mi-1 Glaciation (~23 Ma) records high chemical

578 weathering patterns, but shows the expected excursion towards lighter δ^{13}C and δ^{18}O isotopic

579 values.

580 The reasons for the Cenozoic climate change are hotly debated in the literature, but a strong

581 decrease in atmospheric pCO$_2$ (Pagani et al., 2011; Anagnostou et al., 2016), major tectonic

582 events, such as the collision of India with Asia and progressing exhumation of the Himalaya,

583 as well as re-adjustments in oceanic gateway configurations are widely considered to have

584 altered the global ocean/atmosphere circulation patterns (Caves Rugenstein and Chamberlain,

585 2018). This resulted in large-scale shifts in Earth`s climate at this time, which expressed, for

586 example, in the formation and expansion of the Antarctica ice-sheets and periods of intensified

587 chemical weathering on land (Zachos et al., 2001, and references therein).

588

589 5.6 Hydroclimate and tectonics evolution in Central Asia

590 The links between the regional tectonic evolution and climate change in Central Asia have been

591 extensively studied over the past decades. Recently, Caves Rugenstein and Chamberlain (2018)

592 have concluded Central Asia has received moisture through the mid-latitude westerlies,

593 maintaining stable semi-arid to arid climatic conditions ever since the early Eocene, based on

594 the analysis of δ^{18}O and δ^{13}C isotope systematics of more than 7700 terrestrial authigenic

595 carbonate samples from across Asia. On the contrary, southern Tibet, the central Tibetan

596 Plateau, China and India dominantly received southerly monsoonal moisture, favoring more

597 humid climatic conditions in these regions compared to Central Asia (Ingalls et al., 2018;

598 Sandeep et al., 2018). Our data support this viewpoint: consistently higher δ^{18}O and δ^{13}C values

599 measured for the soil carbonates from the Valley of Lakes (Fig. 8), compared to the surrounding

regions, indicate less precipitation and long-term, sustained arid climatic conditions prevailed

in the late Eocene until the early Miocene (Cerling and Quade, 1993; Kent-Corson et al., 2009;

Takeuchi et al., 2010; Caves et al., 2015; Li et al., 2016; Caves Rugenstein and Chamberlain,

2018). An influence of the height and extension of the Tibetan Plateau or the retreat of the

Parathethys on the hydroclimate in Central Asia at this time (An et al., 2001; Zhang et al., 2009)

is barely documented in the sedimentary record of the Valley of Lakes, but cannot be excluded,

which would express in monsoon-dominant environmental pattern and varying amounts of

precipitation (Zhongshi et al., 2007).

The increase in the δ^{13}C values of the soil carbonates in the Oligocene and the decrease in the

δ^{18}O values in the terminal Oligocene are ultimately linked to coupled effects arising from the

Cenozoic global cooling and the uplift of the Tian Shan and Altai from the early Neogene

onward, which caused changes in the seasonality and quantity of precipitation (Hendrix et al.,

1994; Macaulay et al., 2016; Hellwig et al., 2017; Wang et al., 2020). The resultant effects on

the fractionation of δ^{18}O and δ^{13}C isotopes in soil carbonates are detailed in Caves Rugenstein

and Chamberlain (2018), but are directly related to the development and the establishment of

the Altai rain shadow front. As a consequence, on the leeward side of the Altai, sustained, long-

term drying occurred, which is expressed by systematic changes seen in the isotope profiles

and chemical weathering indices (Fig. 8). Moreover, the progressive uplifting of the Hangay

mountains to the north ever since the early Oligocene also blocked Siberian moisture transport

to the northern Gobi, as it can be inferred from δ^{13}C and δ^{18}O isotope signatures recorded in

paleosol carbonates from different transects at the northern edge of the Gobi Desert and in the

lee of the Altai and Hangay mountains, and consequently contributed to the aridification of this

area (Caves et al., 2014; Sahagian et al., 2016; McDannell et al., 2018). This aridification led

to a concurrent extension of the Gobi Desert, causing shifts and turnovers in mammalian and

gastropod assemblages observed in soils of western Mongolia and in the adjacent eastern

625 Valley of Lakes basin at this time (Neubauer et al., 2013; Harzhauser et al., 2017; Barbolini et

626 al., 2020). We conclude the climatic and environmental evolution of Central Asia in the

627 Cenozoic was closely coupled to global climate change, regional tectonic events and adaptions

628 of the circulation pattern of the westerly winds, transporting less moisture to continental

629 Mongolia, which favored aridification.

630

640

Author contributions

642 A.B. wrote the manuscript. W.E.P. carried out field work and collected the samples. O.W. and

643 S.R. provided the mineralogical and geochemical data. E.A. conducted the discriminant

644 function analyses. K.W. provided the K/Ar ages. A.B., S.B., S.L., W.E.P. and S.R.

645 characterized the palaeo-environment and interpreted the stable δ^{13}C and δ^{18}O isotope records.

646 All authors contributed to the writing of the manuscript.

647

Additional information

649   Supplementary materials are provided in the electronic appendix to this paper. Requests for

650   materials and correspondence should be addressed to A.B.

651

652 **Competing interests**

653 All authors declare no competing interests.

654

655 **References**

656 Abdullayev, E., Baldermann, A., Warr, L.N., Grathoff, G., and Taghiyeva, Y.: New constraints
657   on the palaeo-environmental conditions of the Eastern Paratethys: Implications from the
658   Miocene Diatom Suite (Azerbaijan). Sed. Geol., 411, 105794,
659   https://doi.org/10.1016/j.sedgeo.2020.105794, 2021.
660 An, Z., Kutzbach, J.E., Prell, W.L., and Porter, S.C.: Evolution of Asian monsoons and phased
661   uplift of the Himalaya-Tibetan plateau since Late Miocene times. Nature, 411, 62-66,
662   https://doi.org/10.1038/35075035, 2001.
663 Anagnostou, E., John, E.H., Edgar, K.M., Foster, G.L., Ridgwell, A., Inglis, G.N., Pancost,
664   R.D., Lunt, D.J., and Pearson, P.N.: Changing atmospheric CO_2 concentration was the
665   primary driver of early Cenozoic climate. Nature, 533, 380-384,
666   https://doi.org/10.1038/nature17423, 2016.
667 Badamgarav, D.: A brief lithologo-genetic characteristics of Eocene-Oligocene and Miocene
668   deposits of the Valley of Lakes and Begger depression. In Barsbold, R., and Akhmetiev,
669   M. A. (Eds.). International Geological Correlation Programme, Project 326 Oligocene-
670   Miocene Transitions in the Northern Hemisphere, Excursion Guide-Book Mongolia:
671   Oligocene-Miocene Boundary in Mongolia, 36-39, 1993.
672 Bahlburg, H., and Dobrzinski, N.: A review of the Chemical Index of Alteration (CIA) and its
673   application to the study of Neoproterozoic glacial deposits and climate transitions. In
674   Arnaud, E., Halverson, G.P., and Shields-Zhou, G. (Eds.). The Geological Record of
675   Neoproterozoic Glaciations. Chapter 6, Geol. Soc. Lond. Mem., 36, 81-92,
676   https://doi.org/10.1144/M36.6, 2011.
677 Baldermann, A., Grathoff, G.H., and Nickel, C.: Micromilieu controlled glauconitization in
678   fecal pellets at Oker (Central Germany). Clay Miner., 47, 513-538,
679   https://doi.org/10.1180/claymin.2012.047.4.09, 2012.
680 Baldermann, A., Reinprecht, V., and Dietzel, M.: Chemical weathering and progressing
681   alteration as possible controlling factors for creeping landslides. Sci. Total Environ., 778,
682   146300, https://doi.org/10.1016/j.scitotenv.2021.146300, 2021.
683 Baldermann, A., Dohrmann, R., Kaufhold, S., Nickel, C., Letofsky-Papst, I., and Dietzel, M.:
684   The Fe-Mg-saponite solid solution series – a hydrothermal synthesis study. Clay Miner.,
685   49, 391-415, https://doi.org/10.1180/claymin.2014.049.3.04, 2014.
686 Baldermann, A., Dietzel, M., Mavromatis, V., Mittermayr, F., Warr, L.N., and Wemmer, K.:
687   The role of Fe on the formation and diagenesis of interstratified glauconite-smectite and
688   illite-smectite: A case study of Upper Cretaceous shallow-water carbonates. Chem. Geol.,
689   453, 21-34, https://doi.org/10.1016/j.chemgeo.2017.02.008, 2017.
690 Baldermann, A., Mittermayr, F., Bernasconi, S.M., Dietzel, M., Grengg, C., Hippler, D., Kluge,
691   T., Leis, A., Lin, K., Wang, X., Zünterl, A., and Boch, R.: Fracture dolomite as an archive

of continental palaeo-environmental conditions. Commun. Earth Environ., 1, 35, https://doi.org/10.1038/s43247-020-00040-3, 2020.

Barbolini, N., Woutersen, A., Dupont-Nivet, G., Silvestro, D., Tardif, D., Coster, P.M.C., Meijer, N., Chang, C., Zhang, H.-X., Licht, A., Rydin, C., Koutsodendris, A., Han, F., Rohrmann, A., Liu, X.-J., Zhang, Y., Donnadieu, Y., Fluteau, F., Ladant, J.-B., Le Hir, G., and Hoorn, C.: Cenozoic evolution of the steppe-desert biome in Central Asia. Sci. Adv., 6, 1-16, eabb8227, https://doi.org/10.1126/sciadv.abb8227, 2020.

Bosboom, R., Dupont-Nivet, G., Grothe, A., Brinkhuis, H., Villa, G., Mandic, O., Stoica, M., Huang, W., Yang, W., Guo, Z., and Krijgsman, W.: Linking Tarim sea retreat (west China) and Asian aridification in the late Eocene. Basin Res., 26, 621-640, https://doi.org/10.1111/bre.12054, 2014.

Caves, J.K., Sjostrom, D.J.,Mix, H.T.,Winnick, M.J., and Chamberlain, C.P.: Aridification of Central Asia and uplift of the Altai and Hangay Mountains, Mongolia: stable isotope evidence. Am. J. Sci., 314, 1171-1201, https://doi.org/10.2475/08.2014.01, 2014.

Caves, J.K., Winnick, M.J., Graham, S.A., Sjostrom, D.J., Mulch, A., and Chamberlain, C.P.: Role of the westerlies in Central Asia climate over the Cenozoic. Earth Planet. Sci. Lett., 428, 33-43, https://doi.org/10.1016/j.epsl.2015.07.023, 2015.

Caves Rugenstein, J.K., and Chamberlain, C.P.: The evolution of hydroclimate in Asia over the Cenozoic: A stable-isotope perspective. Earth-Sci. Rev., 185, 1129-1156, https://doi.org/10.1016/j.earscirev.2018.09.003, 2018.

Cerling, T.E.: Late Cenozoic Vegetation Change, Atmospheric CO_2, and Tectonics. In Ruddiman, W.F. (Ed.). Tectonic Uplift and Climate Change. Springer, Boston, MA., 313-327, https://doi.org/10.1007/978-1-4615-5935-1_13, 1993.

Cerling, T., and Quade, J. Stable carbon and oxygen isotopes in soil carbonates. In Swart, P., Lohmann, K., McKenzie, J., and Savin, S. (Eds.). Climate Change in Continental Isotopic Records. American Geophysical Union, Geophysical Monograph, 78, 217-231, https://doi.org/10.1029/GM078p0217, 1993.

Cermeño, P., Falkowski, P.G., Romero, O.E., Schaller, M.F., and Vallina, S.M.: Continental erosion and the Cenozoic rise of marine diatoms. Proc. Natl. Acad. Sci. U.S.A., 112, 4239-4244, https://doi.org/10.1073/pnas.1412883112, 2015.

Chamberlain, C.P., Winnick, M.J., Mix, H.T., Chamberlain, S.D., and Maher, K.: The impact of Neogene grassland expansion and aridification on the isotopic composition of continental precipitation. Global Biogeochem. Cy., 28, 1-13, https://doi.org/10.1002/2014GB004822, 2014.

Chamley, H.: Clay Formation Through Weathering. In Clay Sedimentology. Springer, Berlin, Heidelberg, Germany, 21-50, https://doi.org/10.1007/978-3-642-85916-8_2, 1989.

Cuadros, J.: Modeling of smectite illitization in burial diagenesis environments. Geochim. Cosmochim. Acta, 70, 4181-4195, https://doi.org/10.1016/j.gca.2006.06.1372, 2006.

Daxner-Höck, G., Badamgarav, D., Barsbold, R., Bayarmaa, B., Erbajeva, M., Göhlich, U.B., Harzhauser, M., Höck, V., Höck, E., Ichinnorov, N., Khand, Y., Lopez-Guerrero, P., Maridet, O., Neubauer, T., Oliver, A., Piller, W.E., Tsogtbaatar, K., and Ziegler, R.: Oligocene stratigraphy across the Eocene and Miocene boundaries in the Valley of Lakes (Mongolia). In Daxner-Höck, G., and Göhlich, U. (Eds.). The Valley of Lakes in Mongolia, a key area of Cenozoic mammal evolution and stratigraphy. Paleobiodivers. Paleoenviron., 97, 111-218, https://doi.org/10.1007/s12549-016-0257-9, 2017.

Dupont-Nivet, G., Krijgsman,W., Langereis, C.G., Abels, H.A., Dai, S., and Fang, X.M.: Tibetan plateau aridification linked to global cooling at the Eocene-Oligocene transition. Nature, 445, 635-638, https://doi.org/10.1038/nature05516, 2007.

Fedo, C.M., Nesbitt, H.W., and Young, G.M.: Unraveling the effects of potassium metasomatism in sedimentary rocks and paleosols, with implications of paleoweathering

conditions and provenance. Geology, 23, 921-924, https://doi.org/10.1130/0091-7613(1995)023<0921:UTEOPM>2.3.CO;2, 1995.

Fischer-Femal, and B.J., Bowen, G.J.: Coupled carbon and oxygen isotope model for pedogenic carbonates. Geochim. Cosmochim. Acta, 294, 126-144, https://doi.org/10.1016/j.gca.2020.10.022, 2021.

Gallagher, S.J., Wade, B., Qianyu, L., Holdgate, G.R., Bown, P., Korasidis, V.A., Scher, H., Houben, A.J.P., McGowran, B., and Allan, T.: Eocene to Oligocene high paleolatitude neritic record of Oi-1 glaciation in the Otway Basin southeast Australia. Glob. Planet. Change, 103218, https://doi.org/10.1016/j.gloplacha.2020.103218, 2020.

Grathoff, G.H., and Moore, D.M.: Illite Polytype Quantification Using Wildfire© Calculated X-Ray Diffraction Patterns. Clays Clay Miner., 44, 835-842, https://doi.org/10.1346/CCMN.1996.0440615, 1996.

Guo, Z.T., Sun, B., Zhang, Z.S., Peng, S.Z., Xiao, G.Q.,Ge, J.Y., Hao, Q.Z., Qiao, Y.S., Liang, M.Y., Liu, J.F., Yin, Q.Z., and Wei, J.J.: A major reorganization of Asian climate by the early Miocene. Clim. Past, 4, 153-174, https://doi.org/10.5194/cp-4-153-2008, 2008.

Güven, N., Hower, W.F., and Davies, D.K.: Nature of authigenic illites in sandstone reservoirs. J. Sed. Res., 50, 761-766, https://doi.org/10.1306/212F7ADB-2B24-11D7-8648000102C1865D, 1980.

Harzhauser, M., Daxner-Höck, G., López-Guerrero, P., Maridet, O., Oliver, A., Piller, W.E., Richoz, S., Erbajeva, M.A., and Göhlich, U.B.: The stepwise onset of the Icehouse world and its impact on Oligocene-Miocene Central Asian mammal communities. Sci. Rep., 6, 36169, https://doi.org/10.1038/srep36169, 2016.

Harzhauser, M., Daxner-Höck, Erbajeva, M.A., G., López-Guerrero, P., Maridet, O., Oliver, A., Piller, W.E, Göhlich U.B., and Ziegler, R.: Oligocene and early Miocene biostratigraphy of the Valley of Lakes in Mongolia. In Daxner-Höck, G., and Göhlich, U. (Eds.). The Valley of Lakes in Mongolia, a key area of Cenozoic mammal evolution and stratigraphy. Palaeobiodivers. Palaeoenviron., 97, 219-231, https://doi.org/10.1007/s12549-016-0264-x, 2017.

Hellwig, A., Voigt, S., Mulch, A., Frisch, K., Bartenstein, A., Pross, J., Gerdes, A., and Voigt, T.: Late Oligocene–early Miocene humidity change recorded in terrestrial sequences in the Ili Basin (south-eastern Kazakhstan, Central Asia). Sedimentology, 65, 517-539, https://doi.org/10.1111/sed.12390, 2017.

Hendrix, M., Dumitru, T., and Graham, S.: Late Oligocene-early Miocene unroofing in the Chinese Tian Shan: An early effect of the India-Asia collision. Geology, 22, 487-490, https://doi.org/10.1130/0091-7613(1994)022<0487:LOEMUI>2.3.CO;2, 1994.

Höck, V., Daxner-Höck, G., Schmid, H.P., Badamgarav, D., Frank, W., Furtmüller, G., Montag, O., Barsbold, R., Khand, Y., and Sodov, J.: Oligocene-Miocene sediments, fossils and basalt from the Valley of Lakes (Central Mongolia) – an integrated study. Mitt. Österr. Geol. Ges., 90, 83-125, 1999.

Houben, A.J.P., Bijl, P.K., Pross, J., Bohaty, S.M., Passchier, S., Stickley, C.E., Röhl, U., Sugisaki, S., Tauxe, L., van de Flierdt, T., Olney, M., Sangiorgi, F., Sluijs, A., Escutia, C., and Brinkhuis, H. et al.: Reorganization of Southern Ocean plankton ecosystem at the onset of Antarctic glaciation. Science, 340, 341-344, https://doi.org/10.1126/science.1223646, 2013.

Hubert, J.F., and Filipov, A.J.: Debris-flow deposits in alluvial fans on the west flank of the White Mountains, Owens Valley, California, U.S.A. Sed. Geol., 61, 177-205, https://doi.org/10.1016/0037-0738(89)90057-2, 1989.

Huggett, J., Cuadros, J., Gale, A.S., Wray, D., and Adetunji, J.: Low temperature, authigenic illite and carbonates in a mixed dolomite-clastic lagoonal and pedogenic setting, Spanish

Central System, Spain. Appl. Clay Sci., 132-133, 296-312, https://doi.org/10.1016/j.clay.2016.06.016, 2016.

Ingalls, M., Rowley, D.B., Olack, G., Currie, B.S., Li, S., Schmidt, J.L., Tremblay, M.M., Polissar, P.J., Shuster, D.L., Lin, D., and Colman, A.S.: Paleocene to Pliocene high elevation of southern Tibet: Implications for tectonic models of India-Asia collision, Cenozoic climate, and geochemical weathering. Geol. Soc. Am. Bull., 130, 307-330, https://doi.org/10.1130/B31723.1, 2018.

Kaufman, A.J., and Knoll, A.H.: Neoproterozoic variations in the C-isotopic composition of seawater: stratigraphic and biogeochemical implications. Precambrian Res., 73, 27-49, https://doi.org/10.1016/0301-9268(94)00070-8, 1995.

Kelson, J.R., Huntington, K.W., Breecker, D.O., Burgener, L.K., Gallagher, T.M., Hoke, G.D., and Petersen, S.V.: A proxy for all seasons? A synthesis of clumped isotope data from Holocene soil carbonates. Quat. Sci. Rev., 234, 106259, https://doi.org/10.1016/j.quascirev.2020.106259, 2020.

Kenig, K.: Surface microtextures of quartz grains from Vistulian loesses from selected profiles of Poland and some other countries. Quat. Int., 152-153, 118-135, https://doi.org/10.1016/j.quaint.2005.12.015, 2006.

Kent-Corson, M.L., Ritts, B.D., Zhuang, G., Bovet, P.M., Graham, S.A., and Chamberlain, C.P.: Stable isotopic constraints on the tectonic, topographic, and climatic evolution of the northern margin of the Tibetan Plateau. Earth Planet. Sci. Lett., 282, 158-166, https://doi.org/10.1016/j.epsl.2009.03.011, 2009.

Komar, N., and Zeebe, R.E.: Reconciling atmospheric CO_2, weathering, and calcite compensation depth across the Cenozoic. Sci. Adv., 7, eabd4876, https://doi.org/10.1126/sciadv.abd4876, 2021.

Kukla, T., Winnick, M.J., Maher, K., Ibarra, D.E., and Chamberlain, C.P.: The Sensitivity of Terrestrial $\delta^{18}O$ Gradients to Hydroclimate Evolution. J. Geophys. Res. Atmos., 124, 563-582, https://doi.org/10.1029/2018JD029571, 2019.

Lear, C.H., Bailey, T.R., Pearson, P.N., Coxall, H.K., and Rosenthal, Y.: Cooling and ice growth across the Eocene-Oligocene transition. Geology, 36, 251-254, https://doi.org/10.1130/G24584A.1, 2008.

Li, B., Sun, D., Wang, X., Zhang, Y., Hu, W., Wang, F., Li, Z., Ma, Z., and Liang, B.: $\delta^{18}O$ and $\delta^{13}C$ records from a Cenozoic sedimentary sequence in the Lanzhou Basin, Northwestern China: implications for palaeoenvironmental and palaeoecological changes. J. Asian Earth Sci., 125, 22-36, https://doi.org/10.1016/j.jseaes.2016.05.010, 2016.

Li, H., Liu, X., Tripati, A., Feng, S., Elliott, B., Whicker, C., Arnold, A., and Kelley, A.M.: Factors controlling the oxygen isotopic composition of lacustrine authigenic carbonates in Western China: implications for paleoclimate reconstructions. Sci. Rep., 10, 16370, https://doi.org/10.1038/s41598-020-73422-4, 2020.

Li, Z., Yu, X., Dong, S., Chen, Q., and Zhang, C.: Microtextural features on quartz grains from eolian sands in a subaqueous sedimentary environment: A case study in the hinterland of the Badain Jaran Desert, Northwest China. Aeolian Res., 43, 100573, https://doi.org/10.1016/j.aeolia.2020.100573, 2020.

Lu, H., Wang, X., Wang, X., Chang, X., Zhang, H., Xu, Z., Zhang, W., Wei, H., Zhang, X., Yi, S., Zhang, W., Feng, H., Wang, Y., Wang, Y., and Han, Z.: Formation and evolution of Gobi Desert in central and eastern Asia. Earth-Sci. Rev., 194, 251-263, https://doi.org/10.1016/j.earscirev.2019.04.014, 2019.

Macaulay, E.A., Sobel, E.R., Mikolaichuk, A., Wack, M., Gilder, S.A., Mulch, A., Fortuna, A.B., Hynek, S., and Apayarov, F.: The sedimentary record of the Issyk Kul basin, Kyrgyzstan: climatic and tectonic inferences. Basin Res., 28, 57-80, https://doi.org/10.1111/bre.12098, 2016.

841 McDannell, K.T., Zeitler, P.K., and Idleman, B.D.: Relict Topography Within the Hangay
842   Mountains in Central Mongolia: Quantifying Long-Term Exhumation and Relief Change
843   in an Old Landscape. Tectonics, 37, 2531-2558, https://doi.org/10.1029/2017TC004682,
844   2018.
845 McIntosh, J.A., Tabor, N.J., and Rosenau, A.A.: Mixed-Layer Illite-Smectite in
846   Pennsylvanian-Aged Paleosols: Assessing Sources of Illitization in the Illinois Basin.
847   Minerals, 11, 108, https://doi.org/10.3390/min11020108, 2020.
848 McLennan, S.M.: Weathering and Global Denudation. J. Geol., 101, 100th Anniversary
849   Symposium: Evolution of the Earth's Surface, 295-303,
850   https://www.jstor.org/stable/30081153, 1993.
851 Meenakshi, Shrivastava, J.P., and Chandra, R.: Pedogenically degenerated illite and chlorite
852   lattices aid to palaeoclimatic reconstruction for chronologically constrained (8–130 ka)
853   loess-palaeosols of Dilpur Formation, Kashmir, India. Geosci. Front., 11, 1353-1367,
854   https://doi.org/10.1016/j.gsf.2019.11.007, 2020.
855 Miall, A.D.: The geology of fluvial deposits. Berlin, Germany, Springer, 1-582,
856   https://doi.org/10.1007/978-3-662-03237-4?nosfx=y, 1996.
857 Mudelsee, M., Bickert, T., Lear, C.H., and Lohmann, G.: Cenozoic climate changes: A review
858   based on time series analysis of marine benthic $\delta^{18}O$ records. Rev. Geophys., 52, 333-374,
859   https://doi.org/10.1002/2013RG000440, 2014.
860 Mutz, S.G., Ehlers, T.A., Werner, M., Lohmann, G., Stepanek, C., and Li, J.: Estimates of late
861   Cenozoic climate change relevant to Earth surface processes in tectonically active orogens.
862   Earth Surf. Dynam., 6, 271-301, https://doi.org/10.5194/esurf-6-271-2018, 2018.
863 Nadeau, P.H., Wilson, M.J., McHardy, W.J., and Tait, J.M.: The conversion of smectite to illite
864   during diagenesis: evidence from some illitic clays from bentonites and sandstones.
865   Mineral. Mag., 49, 393-400, https://doi.org/10.1180/minmag.1985.049.352.10, 1985.
866 Neubauer, T.A., Harzhauser, M., Daxner-Höck, G., and Piller, W.E.: New data on the terrestrial
867   gastropods from the Oligocene-Miocene transition in the Valley of Lakes, Central
868   Mongolia. Paleontol. J., 47, 374-385, https://doi.org/10.1134/S003103011304014X, 2013.
869 Nesbitt, H.W., and Young, G.M.: Early Proterozoic climate and plate motions inferred from
870   major element chemistry of lutites. Nature, 299, 715-717,
871   https://doi.org/10.1038/299715a0, 1982.
872 Nesbitt, H.W., and Young, G.M.: Prediction of some weathering trends of plutonic and
873   volcanic rocks based on thermodynamic and kinetic considerations. Geochim.
874   Cosmochim. Acta, 48, 1523-1534, https://doi.org/10.1016/0016-7037(84)90408-3, 1984.
875 Norris, R., Turner, S.K., Hull, P.M., and Ridgwell, A.: Marine Ecosystem Responses to
876   Cenozoic Global Change. Science, 341, 492-498,
877   https://doi.org/10.1126/science.1240543, 2013.
878 Pagani, M., Huber, M., Liu, Z., Bohaty, S.M., Henderiks, J., Sijp, W.P., Krishnan, S., and
879   DeConto, R.M.: The Role of Carbon Dioxide During the Onset of Antarctic Glaciation.
880   Science, 334, 6060, 1261-1264, https://doi.org/10.1126/science.1203909, 2011.
881 Pälike, H., Norris, R.D., Herrle, J.O.,Wilson, P.A., Coxall, H.K., Lear, C., H., Shackleton, N.J.,
882   Tripati, A.K., and Wade, B.S.: The heartbeat of the Oligocene climate system. Science,
883   314, 1894-1898, https://doi.org/10.1126/science.1133822, 2006.
884 Porter, T.M.: The geology, structure and mineralisation of the Oyu Tolgoi porphyry copper-
885   gold-molybdenum deposits, Mongolia: A review. Geosci. Front., 7, 375-407,
886   https://doi.org/10.1016/j.gsf.2015.08.003, 2016.
887 Rafiei, M., Löhr, S., Baldermann, A., Webster, R., and Kong, C.: Quantitative petrographic
888   differentiation of detrital vs diagenetic clay minerals in marine sedimentary sequences:
889   Implications for the rise of biotic soils. Precambrian Res., 350, 105948,
890   https://doi.org/10.1016/j.precamres.2020.105948, 2020.

Richoz, S., Baldermann, A., Frauwallner, A., Harzhauser, M., Daxner-Höck, G., Klammer, D., and Piller, W.E.: Geochemistry and mineralogy of the Oligo-Miocene sediments of the Valley of Lakes, Mongolia. Palaeobiodivers. Palaeoenviron., 97, 233-258, https://doi.org/10.1007/s12549-016-0268-6, 2017.

Roser, B.P., and Korsch, R.J.: Provenance signatures of sandstone-mudstone suites determined using discriminant function analysis of major-element data. Chem. Geol., 67, 119-139, https://doi.org/10.1016/0009-2541(88)90010-1, 1988.

Sahagian, D., Proussevitch, A., Ancuta, L.D., Idleman, B.D., and Zeitler, P.K.: Uplift of Central Mongolia Recorded in Vesicular Basalts. J. Geol., 124, 435-445, https://doi.org/10.1086/686272, 2016.

Sandeep, S., Ajayamohan, R.S., Boos, W.R., Sabin, T.P., and Praveen, V.: Decline and poleward shift in Indian summer monsoon synoptic activity in a warming climate. Proc. Natl. Acad. Sci. U.S.A., 115, 2681-2686, https://doi.org/10.1073/pnas.1709031115, 2018.

Środoń, J.: Mixed-layer illite-smectite in low-temperature diagenesis: data from the Miocene of the Carpathian Foredeep. Clay Miner., 19, 205-215, https://doi.org/10.1180/claymin.1984.019.2.07, 1984.

Sun, J., and Windley, B.F.: Onset of aridification by 34 Ma across the Eocene-Oligocene transition in Central Asia. Geology, 11, 1015-1018, https://doi.org/10.1130/G37165.1, 2015.

Takeuchi, A., Hren, M.T., Smith, S.V., Chamberlain, C.P., and Larson, P.B.: Pedogenic carbonate carbon isotopic constraints on paleoprecipitation: Evolution of desert in the Pacific Northwest, USA, in response to topographic development of the Cascade Range. Chem. Geol., 277, 323-335. https://doi.org/10.1016/j.chemgeo.2010.08.015, 2010.

Teraoka, Y., Suzuki, M., Tungalag, F., Ichinnorov, N., and Sakamaki, Y.: Tectonic framework of the Bayankhongor area, west Mongolia. Bulletin of the Geological Survey of Japan, 47, 447-455, 1996.

Wang, X., Carrapa, B., Sun, Y., Dettman, D.L., Chapman, J.B., Rugenstein, J.K.C., Clementz, M.T., DeCelles, P.G., Wang, M., Chen, J., Quade, J., Wang, F., Li, Z., Oimuhammadzoda, I., Gadoev, M., Lohmann, G., Zhang, X., and Chen, F.: The role of the westerlies and orography in Asian hydroclimate since the late Oligocene. Geology, 48, 728-732, https://doi.org/10.1130/G47400.1, 2020.

Wemmer, K., Steenken, A., Müller, S., de Luchi, M.G.L., and Siegesmund, S.: The tectonic significance of K/Ar illite fine-fraction ages from the San Luis formation (Eastern Sierras Pampeanas, Argentina). Int. J. Earth Sci., 100, 659-669, https://doi.org/10.1007/s00531-010-0629-8, 2011.

Winnick, M.J., Chamberlain, C.P., Caves, J.K., and Welker, J.M.: Quantifying the isotopic "continental effect." Earth Planet. Sci. Lett., 406, 123-133, https://doi.org/10.1016/j.epsl.2014.09.005, 2014.

Xiao, G.Q., Abels, H.A., Yao, Z.Q., Dupont-Nivet, G., and Hilgen, F.J.: Asian aridification linked to the first step of the Eocene-Oligocene climate Transition (EOT) in obliquity-dominated terrestrial records (Xining Basin, China). Clim. Past, 6, 501-513, https://doi.org/10.5194/cp-6-501-2010, 2010.

Zachos, J., Pagani, M., Sloan, L., Thomas, E., and Billups, K.: Trends, rhythms, and aberrations in global climate 65 Ma to present. Science, 292, 686-693, https://doi.org/10.1126/science.1059412, 2001.

Zamanian, K., Lechler, A.R., Schauer, A.J., Kuzyakov, Y., and Huntington, K.W.: The $\delta^{13}C$, $\delta^{18}O$ and Δ_{47} records in biogenic, pedogenic and geogenic carbonate types from paleosol-loess sequence and their paleoenvironmental meaning. Quat. Res., 1-17. https://doi.org/10.1017/qua.2020.109, 2021.

940 Zhang,Y.G., Pagani, M., Liu, Z., Bohaty, S.M., and Deconto, R.: A 40-million-year history of
941   atmospheric CO_2. Philos. T. R. Soc. A, 371, 20130096,
942   https://doi.org/10.1098/rsta.2013.0096, 2013.
943 Zhang, C., Wang, Y., Deng, T., Wang, X., Biasatti, D., Xu, Y., and Li, Q.: C4 expansion in the
944   central Inner Mongolia during the latest Miocene and early Pliocene. Earth Planet. Sci.
945   Lett., 287, 311-319, https://doi.org/10.1016/j.epsl.2009.08.025, 2009.
946 Zhongshi, Z., Wang, H., Guo, Z., and Jiang, D.: What triggers the transition of
947   palaeoenvironmental patterns in China, the Tibetan Plateau uplift or the Paratethys Sea
948   retreat? Palaeogeogr. Palaeoclimatol. Palaeoecol., 245, 317-331,
949   https://doi.org/10.1016/j.palaeo.2006.08.003, 2007.
950 Zorin, Y.A., Belichenko, V.G., Turutanov, E.K., Kozhevnikov, V.M., Ruzhentsev, S.V.,
951   Dergunov, A.B., Filippova, I.B., Tomurtogoo, O., Arvisbaatar, N., Bayasgalan, T.,
952   Biambaa, C., and Khosbayar, P.: The South Siberia-Central Mongolia transect.
953   Tectonophysics, 225, 361-378, https://doi.org/10.1016/0040-1951(93)90305-4, 1993.
954

955

Figure Captions / Table Captions

957 **Table 1:** Compilation of illite polytype quantification and K-Ar ages of grain size sub-fractions

958 of sediments collected from (a) TAT section (~90.5 m), (b) TGR-C section (~78.0 m), (c) SHG-

959 D section (~55.5 m) and (d) TGR-AB section (~35.0 m). The analytical error for the K-Ar age

960 calculations is given on a 95% confidence level (2σ).

Sample	Size fraction [μm]	$A_{(-112)}$ [cps·2θ]	1M [%]	$A_{(114)}$ [cps·2θ]	$2M_1$ [%]	$1M_d$ [%]	K_2O [wt.%]	$^{40}Ar^*$ [nl/g] STP	$^{40}Ar^*$ [%]	Age [Ma]	± 2SD [Ma]
TAT	2-10	-	-	0.054	21	79	2.59	15.45	49.05	176.1	7.1
TAT	1-2	0.006	6	0.040	16	78	2.21	11.58	77.20	155.2	2.6
TAT	< 1	0.012	7	0.023	10	83	3.39	10.75	38.18	95.8	3.2
TGR-C	2-10	-	-	0.038	16	84	2.68	13.98	81.46	155.1	2.9
TGR-C	1-2	-	-	0.031	13	87	3.64	15.80	76.96	129.6	2.4
TGR-C	< 1	0.001	5	0.027	12	95	3.10	12.88	66.83	124.6	1.9
SHG-D	2-10	-	-	0.039	16	84	2.72	14.31	78.74	156.4	2.0
SHG-D	1-2	-	-	0.034	14	86	3.86	15.93	76.09	123.6	3.2
SHG-D	< 1	0.011	6	0.016	8	94	3.49	10.38	70.94	89.9	1.3
TGR-AB	2-10	-	-	0.032	14	86	3.83	17.29	84.05	134.8	3.4
TGR-AB	1-2	-	-	0.027	12	88	3.97	16.63	84.33	125.3	1.8
TGR-AB	< 1	0.032	9	-	0	91	0.64	0.70	10.52	33.9	3.2

961
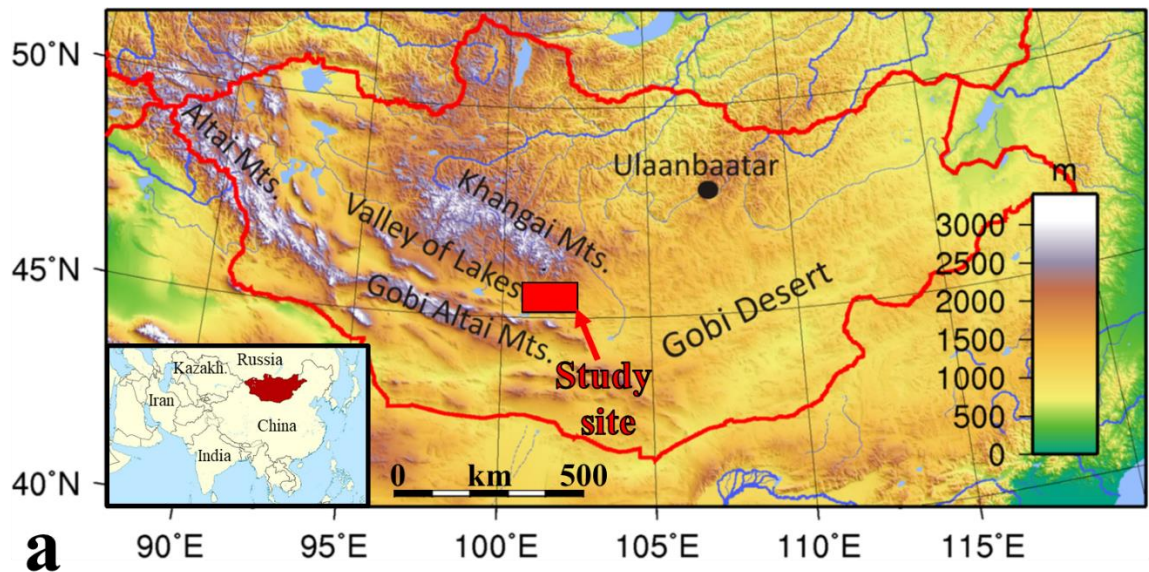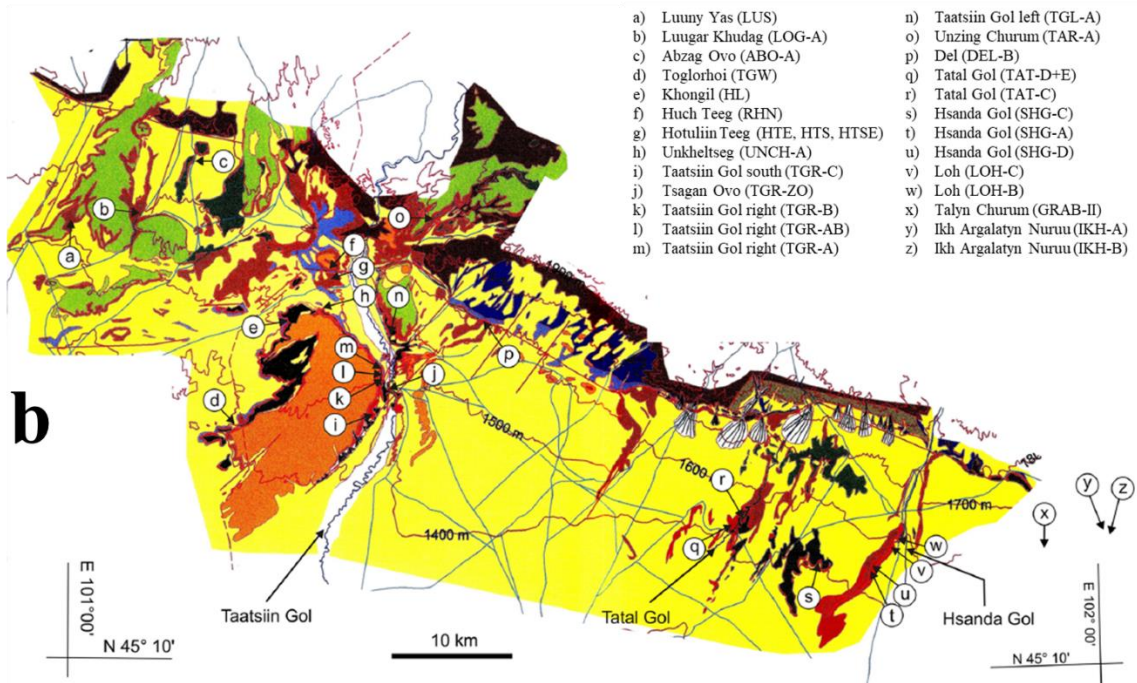
a) Luuny Yas (LUS)
b) Luugar Khudag (LOG-A)
c) Abzag Ovo (ABO-A)
d) Toglorhoi (TGW)
e) Khongil (HL)
f) Huch Teeg (RHN)
g) Hotuliin Teeg (HTE, HTS, HTSE)
h) Unkheltseg (UNCH-A)
i) Taatsiin Gol south (TGR-C)
j) Tsagan Ovo (TGR-ZO)
k) Taatsiin Gol right (TGR-B)
l) Taatsiin Gol right (TGR-AB)
m) Taatsiin Gol right (TGR-A)
n) Taatsiin Gol left (TGL-A)
o) Unzing Churum (TAR-A)
p) Del (DEL-B)
q) Tatal Gol (TAT-D+E)
r) Tatal Gol (TAT-C)
s) Hsanda Gol (SHG-C)
t) Hsanda Gol (SHG-A)
u) Hsanda Gol (SHG-D)
v) Loh (LOH-C)
w) Loh (LOH-B)
x) Talyn Churum (GRAB-II)
y) Ikh Argalatyn Nuruu (IKH-A)
z) Ikh Argalatyn Nuruu (IKH-B)

Legend

Qaternary
Tuyn Gol Fm.
Loh Fm.
Hsanda Gol Fm.
Tsagan Ovo Fm.
Mesozoic sediments
Neoarchean basement
Pa!aeozoic basement
Basalt III (M-Miocene)
Basalt I+II (Oligocene)

Figure 1: (a) Location of the study site in the Taatsiin Gol region, a part of the Valley of Lakes, in Mongolia (Central Asia). Altitude in meters is indicated on the right. (b) Geological map of the Taatsiin Gol area within the Valley of Lakes with the sampling sites marked in alphabetical order (modified after Daxner-Höck et al., 2017).
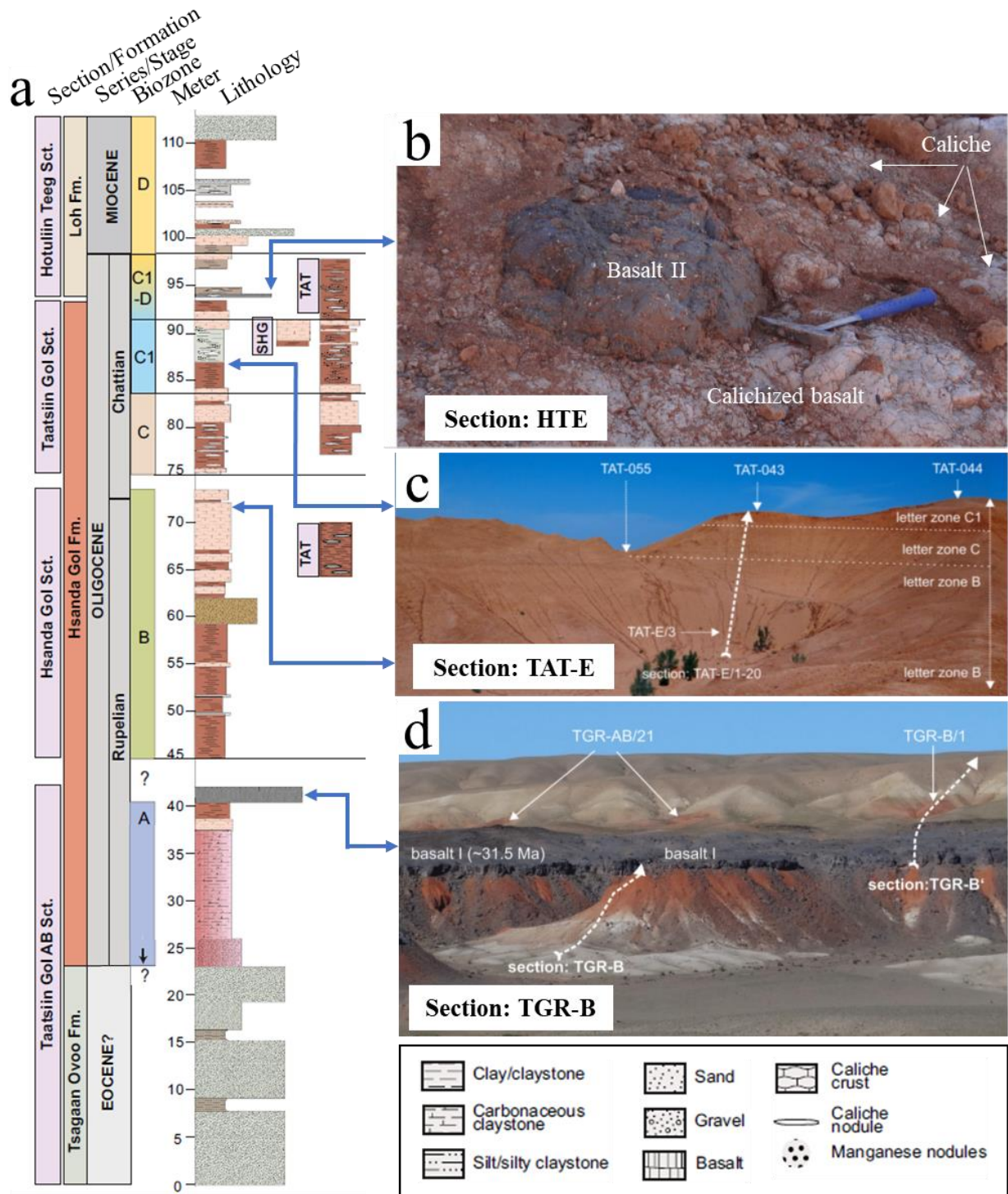
Figure 2: (a) Integrated lithostratigraphic profile of the investigated sedimentary succession from the Taatsiin Gol region, Valley of Lakes (modified after Richoz et al., 2017), with biozonation (modified after Harzhauser et al., 2017). (b-d) Field impressions of the sections Hotuliin Teeg (HTE) with calichized basalt II group, Tatal Gol (TAT-E) sediments and Taatsiin Gol right (TGR-B) section with basalt I group (modified after Daxner-Höck et al., 2017).

35
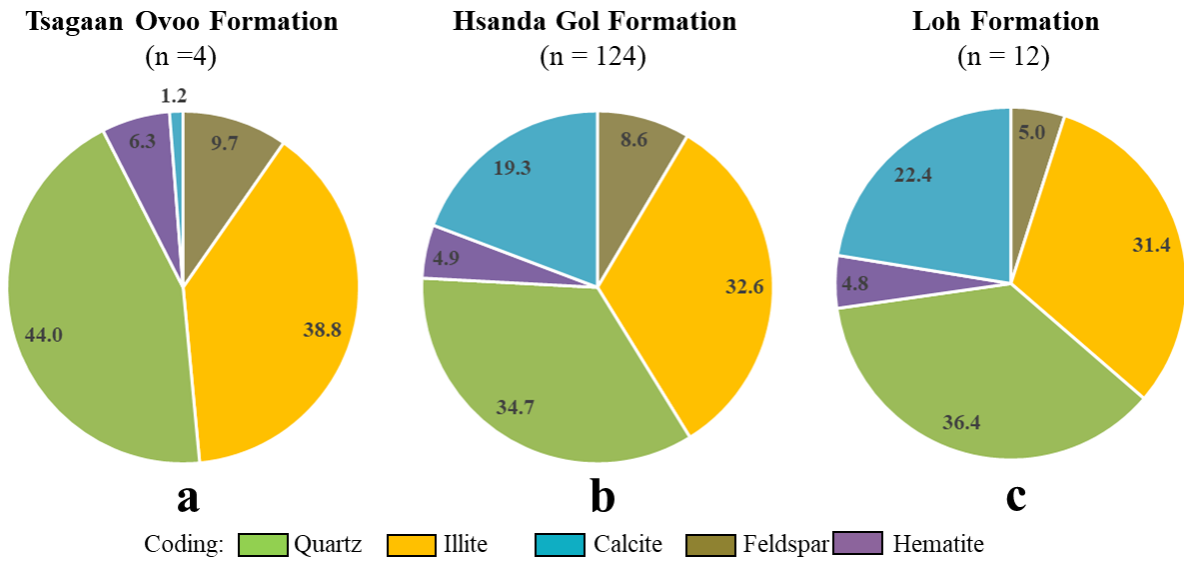
Figure 3: Averaged mineralogical composition (in wt%) of the sediments from the (a) upper Eocene Tsagaan Ovoo Formation, (b) Oligocene Hsanda Gol Formation and (c) lower Miocene Loh Formation from the Valley of Lakes, determined by XRD analysis.
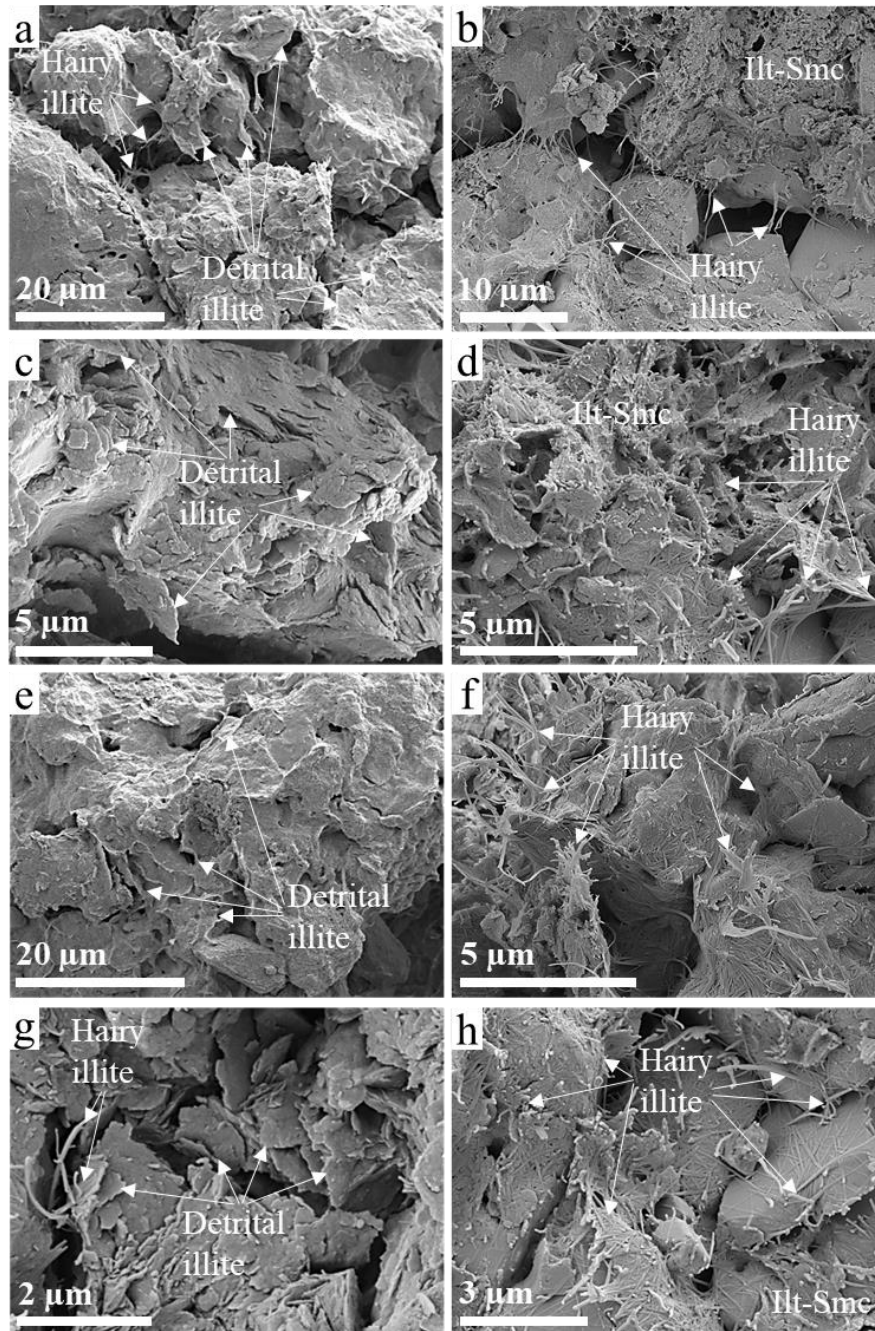
Figure 4: Secondary electron images of partly calichized and illitized silty to sandy deposits from the of the Oligocene Hsanda Gol Formation, Valley of Lakes, collected from (a-b) TAT section (~90.5 m), (c-d) TGR-C section (~78.0 m), (e-f) SHG-D section (~55.5 m) and (g-h) TGR-AB section (~35.0 m). The detrital illite/muscovite (left panel) occurs as coarse, rounded or pseudohexagonal platelets, whereas authigenic illite-smectite (Ilt-Smc) and hairy illite (right panel) appear either as fine, flaky to irregular particles or as long, but thin laths and fibers, both covering detrital grains or growing into the open pores.
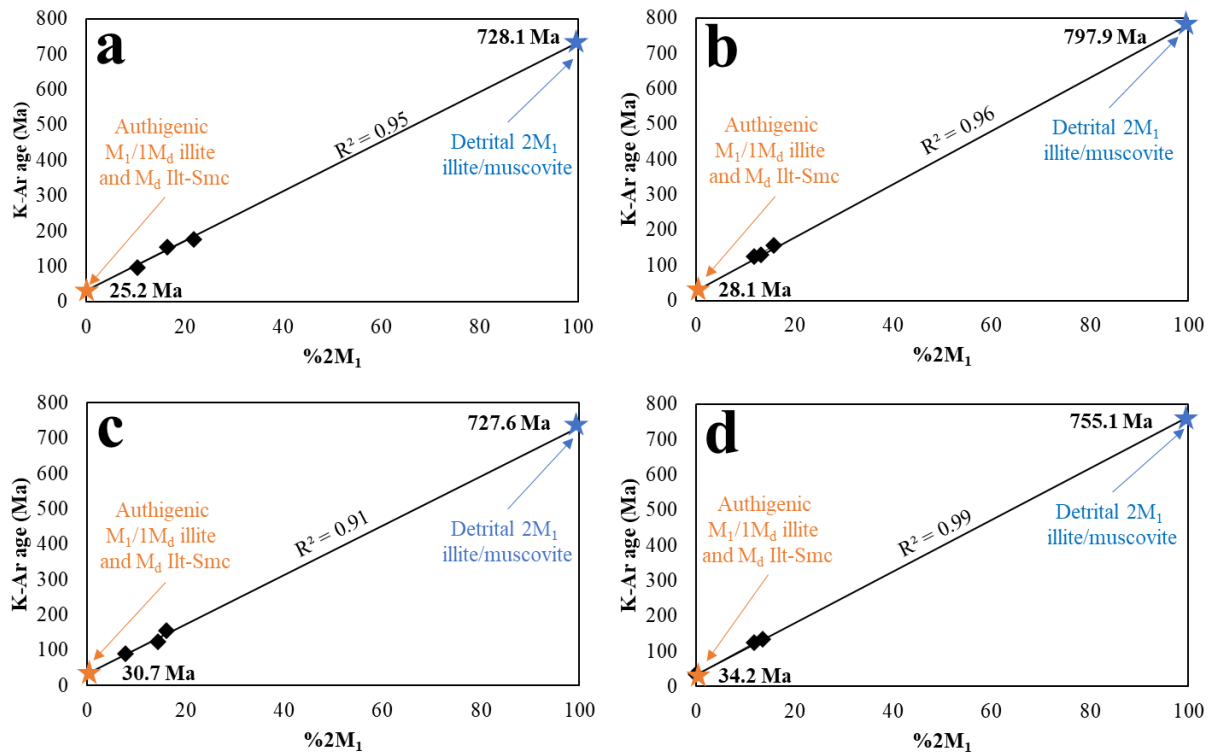
Figure 5: Crystallization ages of detrital $2M_1$ illite/muscovite and of authigenic $1M_d/1M$ illite and illite-smectite (Ilt-Smc) fr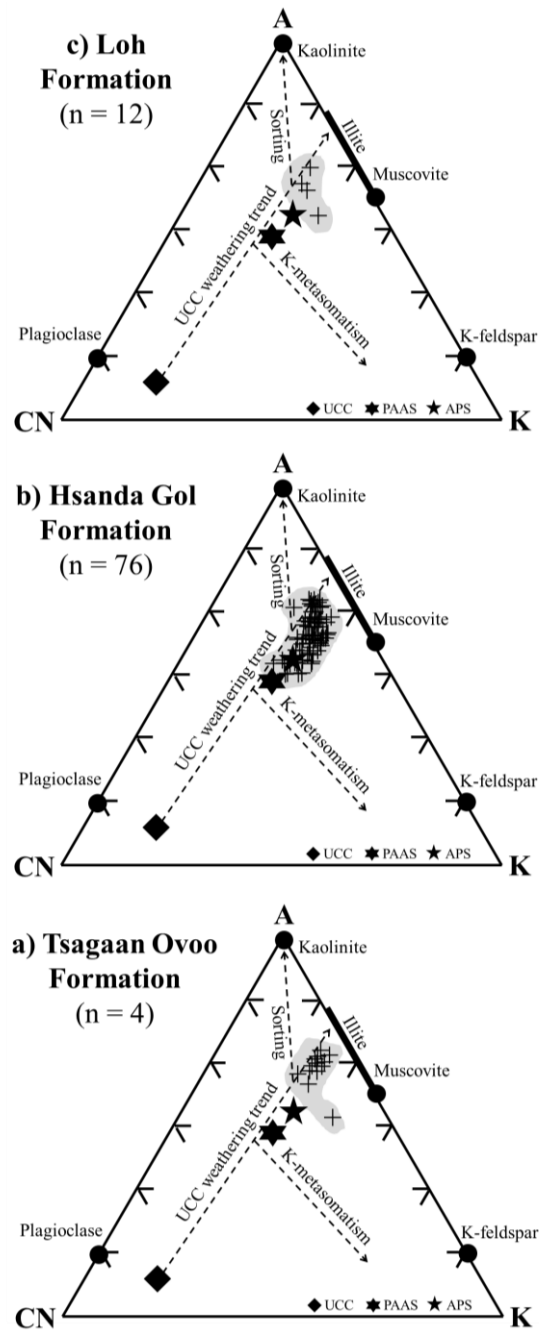om the Valley of Lakes, calculated for sediments collected from (a) TAT section (~90.5 m), (b) TGR-C section (~78.0 m), (c) SHG-D section (~55.5 m) and (d) TGR-AB section (~35.0 m) using illite polytype quantification and K-Ar age systematics of different grain size sub-fractions (from left to right: < 1 μm, 1-2 μm and 2-10 μm).

Figure 6: Al$_2$O$_3$-(CaO*+Na$_2$O)-K$_2$O (A-CN-K) ternary diagram of Nesbitt and Young (1984) showing the compositional rang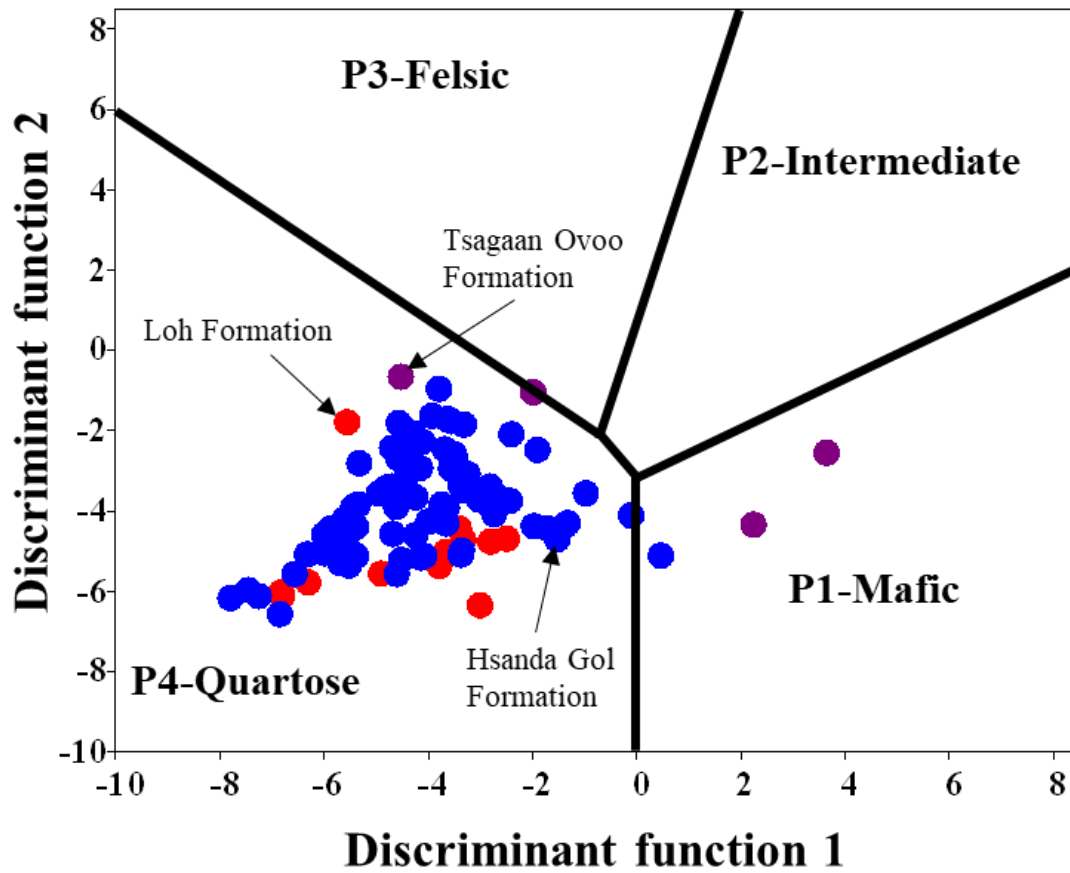es of sediments from the Valley of Lakes, from the bottom to the top, from (a) upper Eocene Tsagaan Ovoo Formation, (b) Oligocene Hsanda Gol Formation and (c) lower Miocene Loh Formation. Note that most samples are shifted to the K pole of the diagram, which indicates a post-depositional enrichment of K$_2$O due to illitization. The composition of Upper Contin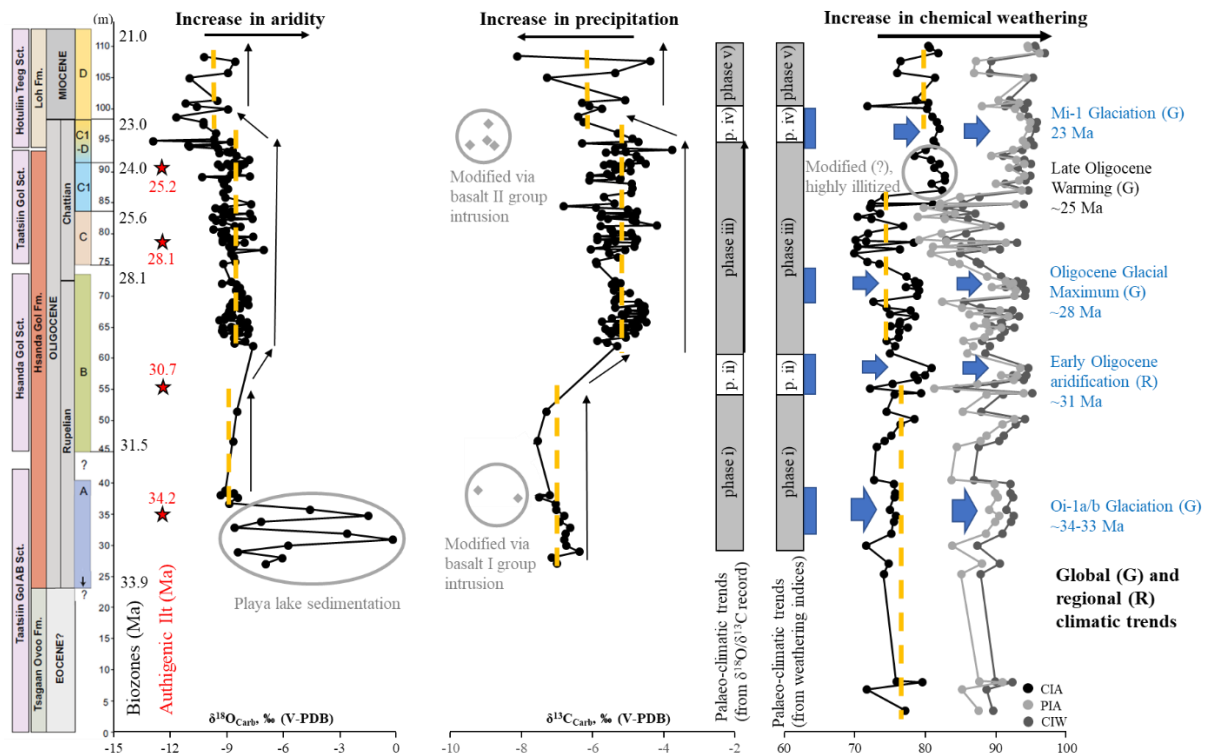ental Crust (UCC), Average Proterozoic Shale (APS) and Post-Archean Australian Shale (PAAS) are included for comparison.

Figure 7: Discrimination plot of discriminant function 1 and 2 indicating a narrow provenance range (mainly type P4-quartzose) for the sediments from the Valley of Lakes, Mongolia.

Figure 8: Lithostratigraphic framework of the sediments from the Valley of Lakes (Mongolia, Central Asia) showing the biozonation (modified after Harzhauser et al., 2017) and formation ages of authigenic illitic (Ilt) phases obtained in this study (red asterisks), as well as soil carbonate $\delta^{18}O$ and $\delta^{13}C$ isotope profiles and shifts in the silicate mineral-derived chemical weathering indicators. Note that these hydroclimate proxies are inversely correlated and follow long-term trends (indicated by orange dashed lines) in aridification or gain of humidity in this region (indicated by black arrows). Increased chemical weathering degrees (highlighted with blue bars and blue arrows) coincide with glaciation events documented in time-equivalent marine deep-sea deposits (Zachos et al., 2001; Gallagher et al., 2020). Samples and intervals outlined with grey circles are most likely modified due to the flows of the basalt I and II groups or local strong illitization, and are therefore excluded from the palaeo-climatic interpretation.